Coalescence of binary neutron stars in a scalar-tensor theory of gravity

Masaru Shibata[1], Keisuke Taniguchi[2], Hirotada Okawa[3], Alessandra Buonanno[4]
[1]*Yukawa Institute for Theoretical Physics, Kyoto University, Kyoto 606-8502, Japan*
[2]*Graduate School of Arts and Sciences, University of Tokyo, Komaba, Meguro, Tokyo 153-8902, Japan*
[3]*CENTRA, Departamento de Física, Instituto Superior Técnico,*
Universidade Técnica de Lisboa - UTL,Avenida Rovisco Pais 1, 1049 Lisboa, Portugal and
[4]*Maryland Center for Fundamental Physics and Joint Space-Science Institute,*
Department of Physics, University of Maryland, College Park, MD 20742, USA
(Dated: October 7, 2013)

We carry out numerical-relativity simulations of coalescing binary neutron stars in a scalar-tensor theory that admits spontaneous scalarization. We model neutron stars with realistic equations of state. We choose the free parameters of the theory taking into account the constraints imposed by the latest observations of neutron-star–white-dwarf binaries with pulsar timing. We show that even within those severe constraints, scalarization can still affect the evolution of the binary neutron stars not only during the late inspiral, but also during the merger stage. We also confirm that even when both neutron stars have quite small scalar charge at large separations, they can be strongly scalarized *dynamically* during the final stages of the inspiral. In particular, we identify the binary parameters for which scalarization occurs either during the late inspiral or only after the onset of the merger when a remnant, supramassive or hypermassive neutron star is formed. We also discuss how those results can impact the extraction of physical information on gravitational waves once they are detected.

PACS numbers: 04.25.D-, 04.30.-w, 04.40.Dg

I. INTRODUCTION

Coalescing binary neutron stars are among the most promising sources for the next-generation of kilometer-size gravitational-wave detectors such as advanced LIGO, advanced Virgo, and KAGRA (or LCGT) [1]. These detectors will be operational within the next five years. Based on the current estimates of event rates from binary neutron stars, we expect that advanced detectors will observe ~ 0.4–400 events per year at the distance of 200 Mpc [3, 4], which is the average distance the advanced detectors will be sensitive to. Thus, likely, the first detection(s) of gravitational waves will happen before the end of this decade by observing gravitational waves emitted by coalescing binary neutron stars.

One of the most interesting payoff of gravitational-wave observations is the exploration of the validity of general relativity in the strong-field dynamical regime. Scalar-tensor gravity is the simplest and most well motivated class of alternative theories to general relativity — for example it has been postulated as a possible low-energy limit of string theory. The most popular scalar-tensor gravity theory was proposed by Jordan-Fierz-Brans-Dicke (JFBD) [5–7] (see also Ref. [8] for a review). The JFBD theory depends on one single, constant parameter, $\omega_{\rm BD}$, which determines the coupling strength between the gravitational and scalar fields. This parameter has been strongly constrained by a number of observations and experiments [9]. In particular, the experiments performed using the Cassini spacecraft [10] imply $\omega_{\rm BD} \gtrsim 4\times 10^4$.

There exist generalizations of the JFBD scalar-tensor theory that still satisfy the weak but not the strong equivalence principle and have richer phenomenology. An interesting class of theories is the one proposed by Damour and Esposito-Farése [11–13] in the early 90s. In their models, $\omega_{\rm BD}$ is no longer constant but depends on the scalar field ϕ, i.e., $\omega(\phi)$. The latter can be chosen to be sufficiently large in the weakly gravitating field of a star, such as the Sun, so that it satisfies experimental tests [10], but it may be significantly small, e.g., $\omega = \mathcal{O}(1)$, in the strongly gravitating field in the vicinity of massive neutron stars. Because gravitational-wave observations will probe the strong-field dynamical regime of coalescing neutron stars, they could detect or constrain those alternative theories to general relativity. Other modified theories to general relativity have been proposed in the literature [9]. Among them, the $f(R)$ theories were introduced as an alternative to the conventional dark-energy model, to provide an explanation for the acceleration of the Universe. Those theories can be recast into the form of a scalar-tensor theory [14]. The Einstein-aether theory [15] violates Lorentz symmetry due to the existence of a preferred time direction at each spacetime points. The free parameters in the Einstein-aether theory have been constrained with a variety of observations [16].

Coalescing compact-body binaries offer a unique laboratory to test alternative theories to general relativity through gravitational-wave observations. To reach this goal, the two-body dynamics and gravitational-wave emission in modified theories have been computed analytically, in an approximated way, via the post-Newtonian framework [8, 17–19], and more recently, also numerically, solving the field equations with all the nonlinearities [20–22]. Here we focus on the scalar-tensor theory by Damour and Esposito-Farése (DEF) [11–13] and study its strong-field dynamical regime by performing numerical-relativity simulations of coalescing binary neutron stars. As we shall see below, the possibility of observing deviations from general relativity in the gravitational waveforms in those theories may be possible because (i) neutron stars in binaries can have large component masses (i.e., larger than the canonical value $1.4M_\odot$), (ii) the merger remnant is a neutron star with a large mass, (iii) scalarization enhances the gravitational interaction between the two neutron stars, reducing the time to merger [21], and (iv) neutron stars can be strongly

scalarized during the last stages of the inspiral and plunge even if one or both neutron stars [21] had a quite small scalar charge at much larger separations. This latter phenomenon open the possibility of observing deviations from general relativity via direct detection of gravitational waves from binary neutron stars even if the indirect observation of gravitational-waves via pulsar timing [24, 25] did not detect any deviation at much larger separations.

Reference [21] has recently performed numerical-relativity simulations of binary neutron stars in the DEF theory. Here, we shall investigate in more detail several interesting features found in Ref. [21] and improve their work in different directions. First, we start the numerical simulations from quasiequilibrium configurations that consistently include also the scalar field. By contrast, Ref. [21] set initially the scalar field to zero. Second, Ref. [21] employed a simple polytropic equation of state (EOS) with $\Gamma = 2$ for the neutron star. Whereas this choice of the EOS may be acceptable for a qualitative study, it does not describe very realistic neutron stars. As we shall see below, the degree of scalarization in neutron stars does depend on the EOS. Thus, if we want to make realistic predictions, we need to employ realistic EOS, which is what we do here. Third, as a first study, Ref. [21] focused only on the late stages of inspiral and plunge. They did not investigate in any detail the merger phase. As we shall find below, the frequency of gravitational waves emitted by the newly-born, massive neutron star can be strongly modified due to scalarization — for example the frequency characteristics not only depend on the EOS [26, 27] but also on the scalar field. Finally, an important difference between Ref. [21] and our work is that we carry out the numerical simulation in the so-called Jordan frame, while Ref. [21] employed the so-called Einstein frame.

This paper is organized as follows. In Sec. II, we describe the basic equations of the scalar-tensor model employed here and the numerical methods used to carry out the numerical simulations. We also briefly discuss how we build the quasiequilibrium initial conditions (for more details see Ref. [23]). In Sec. III, we discuss the phenomenon of spontaneous scalarization for a single neutron star and describe how we choose the free parameters in our scalar-tensor model taking into account constraints from pulsar-timing observations of binary pulsars [24, 25]. In addition, we explain how dynamical scalarization can occur in close binaries of neutron stars. In Sec. IV, we present the results of the numerical simulations and discuss the effect of scalarization on the gravitational waveforms during the last stages of inspiral, plunge, and merger. Section V is devoted to a summary and a discussion of future studies. Finally, in Appendix A we check the validity of the numerical code developed for scalar-tensor theories by performing simulations of spherical neutron stars. In Appendix B, we study the numerical convergence of the simulations and we estimate the numerical errors due to resolution.

Throughout this paper, we employ the geometrical units $c = 1 = G$ where c and G are the speed of light and bare gravitational constant, respectively. Subscripts a, b, $c, \cdots$ denote the spacetime components while i, j, k, and l denote the spatial components, respectively.

II. NUMERICAL SIMULATIONS IN SCALAR-TENSOR GRAVITY

A. Basic equations

We briefly summarize the basic equations of the JFBD-type scalar-tensor theory in the 3+1 formulation. Scalar-tensor theories of the simplest form are composed of the spacetime metric g_{ab} and a single real scalar field ϕ that determines the strength of the coupling between the matter and the gravitational field. The action in the so-called Jordan frame is:

$$S = \frac{1}{16\pi G}\int d^4x\sqrt{-g}\left[\phi\mathscr{R} - \frac{\omega(\phi)}{\phi}g^{ab}\nabla_a\phi\,\nabla_b\phi\right] - \int d^4x\sqrt{-g}\rho(1+\varepsilon), \tag{1}$$

where $\mathscr{R}$ is the Ricci scalar associated with g_{ab}, ρ is the rest-mass density, and ε is the specific internal energy. We note that in this paper, we describe the matter component with a perfect fluid. The equations of motion are

$$G_{ab} = 8\pi\phi^{-1}T_{ab} + \omega(\phi)\phi^{-2}\left[(\nabla_a\phi)\nabla_b\phi - \frac{1}{2}g_{ab}(\nabla_c\phi)\nabla^c\phi\right] + \phi^{-1}(\nabla_a\nabla_b\phi - g_{ab}\Box_g\phi), \tag{2}$$

$$\Box_g\phi = \frac{1}{2\omega(\phi)+3}\left[8\pi T - \frac{d\omega}{d\phi}(\nabla_c\phi)\nabla^c\phi\right], \tag{3}$$

$$\nabla_a T^a_{\ b} = 0, \tag{4}$$

where G_{ab} and ∇_a are the Einstein tensor and covariant derivative associated with g_{ab}, $\Box_g$ is $\nabla_a\nabla^a$, $\omega(\phi)$ determines the strength of the coupling between the gravitational and scalar fields, and T_{ab} is the stress-energy tensor of the perfect fluid with $T = T_a^{\ a}$. The matter is coupled only to the gravitational field in the Jordan frame, as Eq. (4) shows, and hence, the equations for the perfect fluid are the same as those in general relativity in this frame. In the following, we write Eqs. (2) and (3) in the 3+1 formulation.

The basic equations in the 3+1 formulation for the gravitational field are derived simply by contracting $n^a n^b$, $n^a\gamma^b_i$, and $\gamma^a_i\gamma^b_j$ with Eq. (2). Here, γ_{ab} denotes the spatial metric, and n^a is the unit normal to spatial hypersurfaces. A straightforward calculation yields the Hamiltonian constraint as

$$R_k^{\ k} + K^2 - K_{ij}K^{ij} = 16\pi\phi^{-1}\rho_{\rm h} + \omega\phi^{-2}[\Pi^2 + (D_i\phi)D^i\phi] + 2\phi^{-1}(-K\Pi + D_iD^i\phi), \tag{5}$$

where $R_k^{\ k}$ is the three-dimensional Ricci scalar, D_i the covariant derivative with respect to the spatial metric, $\rho_{\rm h} := T_{ab}n^a n^b$, $\Pi := -n^a\nabla_a\phi$, and K_{ij} is the extrinsic curvature with K its trace.

The momentum constraint is written as

$$D_i K^i{}_j - D_j K = 8\pi\phi^{-1} J_j + \omega\phi^{-2}\Pi D_j\phi + \phi^{-1}(D_j\Pi - K^i{}_j D_i\phi), \tag{6}$$

where $J_i := -T_{ab}n^a\gamma^b_i$.

Finally, the evolution equation is

$$\begin{aligned}\partial_t K_{ij} &= \alpha R_{ij} - 8\pi\alpha\phi^{-1}\Big[S_{ij} - \frac{1}{2}\gamma_{ij}(S-\rho_{\rm h})\Big] \\ &+ \alpha(-2K_{ik}K_j{}^k + KK_{ij}) \\ &- D_iD_j\alpha + \beta^k D_k K_{ij} + K_{ik}D_j\beta^k + K_{kj}D_i\beta^k \\ &- \alpha\omega\phi^{-2}(D_i\phi)D_j\phi - \alpha\phi^{-1}\Big[D_iD_j\phi - K_{ij}\Pi \\ &+ \frac{1}{2(2\omega+3)}\gamma_{ij}\Big\{8\pi T + \frac{d\omega}{d\phi}(\Pi^2 - (D_k\phi)D^k\phi)\Big\}\Big],\end{aligned} \tag{7}$$

where R_{ij} is the spatial Ricci tensor and $S_{ij} := T_{ab}\gamma^a_i\gamma^b_j$ with S its trace. Equation (7) together with the Hamiltonian constraint yields the following evolution equation for K:

$$\begin{aligned}(\partial_t - \beta^k\partial_k)K &= 4\pi\alpha\phi^{-1}(S+\rho_{\rm h}) + \alpha K_{ij}K^{ij} - D_iD^i\alpha \\ &+ \alpha\omega\phi^{-2}\Pi^2 + \alpha\phi^{-1}\Big[D_iD^i\phi - K\Pi \\ &- \frac{3}{2(2\omega+3)}\Big\{8\pi T + \frac{d\omega}{d\phi}(\Pi^2 - (D_k\phi)D^k\phi)\Big\}\Big].\end{aligned} \tag{8}$$

The left-hand side of Eq. (3) is recast in the following form

$$\Box_g\phi = D_aD^a\phi + (D_a\ln\alpha)D^a\phi + (\nabla_a n^a)\Pi + n^a\partial_a\Pi, \tag{9}$$

and then Eq. (3) is re-written into a set of equations that are first order in the time derivatives

$$(\partial_t - \beta^k\partial_k)\phi = -\alpha\Pi, \tag{10}$$

$$\begin{aligned}(\partial_t - \beta^k\partial_k)\Pi &= -\alpha D_iD^i\phi - (D_i\alpha)D^i\phi + \alpha K\Pi \\ &+ \frac{\alpha}{2\omega+3}\Big[8\pi T - \frac{d\omega}{d\phi}(\nabla_c\phi)\nabla^c\phi\Big].\end{aligned} \tag{11}$$

The evolution equations for the gravitational fields are solved in the Baumgarte-Shapiro-Shibata-Nakamura formalism [28, 29] with the moving-puncture gauge [30–32] as we have been doing in general relativity [33]. In particular, we evolve the conformal factor $W := \gamma^{-1/6}$, the conformal metric $\tilde{\gamma}_{ij} := \gamma^{-1/3}\gamma_{ij}$, the trace of the extrinsic curvature K, the conformally-weighted trace-free part of the extrinsic curvature $\tilde{A}_{ij} := \gamma^{-1/3}(K_{ij} - K\gamma_{ij}/3)$, and the auxiliary variable $\tilde{\Gamma}^i := -\partial_j\tilde{\gamma}^{ij}$. Introducing the auxiliary variable B^i and a parameter η_s, which we typically set to be $\sim m^{-1}$, m being the total mass of the system, we employ the moving-puncture gauge in the form [34]

$$(\partial_t - \beta^j\partial_j)\alpha = -2\alpha K, \tag{12}$$

$$(\partial_t - \beta^j\partial_j)\beta^i = (3/4)B^i, \tag{13}$$

$$(\partial_t - \beta^j\partial_j)B^i = (\partial_t - \beta^j\partial_j)\tilde{\Gamma}^i - \eta_s B^i. \tag{14}$$

The spatial derivative is evaluated by a fourth-order central finite difference except for the advection terms, which are evaluated by a fourth-order noncentered finite difference. We employ a fourth-order Runge-Kutta method for the time evolution. For the scalar field, we use the same scheme as those for the tensor field because the structure of the equations is essentially the same.

To solve the hydrodynamics equations, we evolve $\rho_* := \rho\alpha u^t W^{-3}$, $\hat{u}_i := hu_i$, and $e_* := h\alpha u^t - P/(\rho\alpha u^t)$ with u^a, P, h being the four velocity, pressure, and specific enthalpy. The advection terms are handled with a high-resolution central scheme by Kurganov and Tadmor [35] with a third-order piecewise parabolic interpolation for the cell reconstruction. For the EOS, we decompose the pressure and specific internal energy into cold and thermal parts as

$$P = P_{\rm cold} + P_{\rm th}\ ,\ \varepsilon = \varepsilon_{\rm cold} + \varepsilon_{\rm th}. \tag{15}$$

Here, $P_{\rm cold}$ and $\varepsilon_{\rm cold}$ are functions of ρ, and their forms are determined by nuclear-theory-based zero-temperature EOSs. Specifically, the cold parts of both variables are determined using the piecewise polytropic EOS (see, e.g., Ref. [36] for details).

Then the thermal part of the specific internal energy is defined from ε as $\varepsilon_{\rm th} := \varepsilon - \varepsilon_{\rm cold}$. Because $\varepsilon_{\rm th}$ vanishes in the absence of shock heating, $\varepsilon_{\rm th}$ is regarded as the finite-temperature part. In this paper, we adopt a Γ-law ideal gas EOS

$$P_{\rm th} = (\Gamma_{\rm th} - 1)\rho\varepsilon_{\rm th}, \tag{16}$$

to determine the thermal part of the pressure, and choose $\Gamma_{\rm th}$ equal to 1.8 following [37].

B. Choice of the functional form of ω and equations for the scalar field

To obtain a scalar-tensor model with spontaneous scalarization we use the following function for $\omega(\phi)$

$$\frac{1}{\omega(\phi)+3/2} = B\ln\phi, \tag{17}$$

where B is a free parameter. For reasons that will become clear below we also introduce the field φ defined as $\phi = \exp(\varphi^2/2)$. If we want to compare our model (17) with the one used in Refs. [11–13], we should consider that Damour and Esposito-Farése worked in the Einstein frame, while we use the Jordan frame. In the Einstein frame one introduces the field $\bar{\varphi}$ [1], which is related to ϕ through the following equations

$$\phi = \frac{1}{A^2(\bar{\varphi})}, \tag{18}$$

$$\alpha^2(\bar{\varphi}) = \left[\frac{\partial\ln A(\bar{\varphi})}{\partial\bar{\varphi}}\right]^2 = \frac{1}{2\omega(\phi)+3}, \tag{19}$$

[1] We note that in Refs. [11–13] the authors denote the scalar field $\bar{\varphi}$ with φ.

The simplest function that the authors of Refs. [11–13] used to generate spontaneous scalarization is

$$A(\bar{\varphi}) = e^{\frac{1}{2}\beta\bar{\varphi}^2}. \tag{20}$$

We have $\alpha_0 = (\partial \ln A/\partial\bar{\varphi})_{\bar{\varphi}=\bar{\varphi}_0} = \beta\bar{\varphi}_0$ and $\beta_0 = (\partial^2 \ln A/\partial\bar{\varphi}^2)_{\bar{\varphi}=\bar{\varphi}_0} = \beta$. Moreover, $\varphi = \sqrt{-2\beta}\bar{\varphi}$, so we find that $B = -2\beta$. In summary, the parameters $(\bar{\varphi}_0, \beta_0)$ in Refs. [11–13] play a role similar to the parameters (φ_0, B) in this paper. As in previous works [11–13, 21], we focus in this paper on the cases with $B \lesssim 10$.

We note that when ω =const, the scalar-field equation (3) is a simple wave equation for ϕ, i.e., it is a hyperbolic partial differential equation and it has a well-posed initial value problem. However, when ω is not a constant, such as in Eq. (17), ϕ does not obey a wave equation because of the presence of the second term in the right-hand side of Eq. (3). To derive a wave equation, at least in the far zone, it is convenient to introduce φ which is related to ϕ by

$$\phi = \exp(\varphi^2/2). \tag{21}$$

Then, the equation for φ reduces to

$$\Box_g\varphi = 2\pi BT\varphi\exp(-\varphi^2/2) - \varphi(\nabla_c\varphi)\nabla^c\varphi. \tag{22}$$

In the far zone, the right-hand side of this equation falls off sufficiently rapidly, and hence, φ obeys a wave equation in the far zone.

We find it convenient to introduce a new variable $\Phi := -n^a\nabla_a\varphi$ and replace Eqs. (10) and (11) by

$$(\partial_t - \beta^k\partial_k)\varphi = -\alpha\Phi, \tag{23}$$

$$\begin{aligned}(\partial_t - \beta^k\partial_k)\Phi = &-\alpha D_iD^i\varphi - (D_i\alpha)D^i\varphi \\ &-\alpha\varphi(\nabla_a\varphi)\nabla^a\varphi + \alpha K\Phi \\ &+2\pi\alpha BT\varphi\exp(-\varphi^2/2).\end{aligned} \tag{24}$$

Here, the boundary condition for $r\to\infty$ should be $\varphi = \varphi_0 \neq 0$ where $\phi_0 = \exp(\varphi_0^2/2)$. In addition, we have $\Pi = \phi\varphi\Phi$ and $D_i\phi = \phi\varphi D_i\varphi$, and, in a straightforward manner, we can replace (ϕ, Π) to (φ, Φ) in all the gravitational-field equations.

Lastly, since in the far zone $\phi = e^{\varphi^2/2} \to 1 + \varphi^2/2$, the asymptotic wave component of ϕ is $1 + \varphi_0^2/2 + \varphi_0(\varphi - \varphi_0) + O[(\varphi - \varphi_0)^2]$. As we shall find in Sec. III, because of observational constraints φ_0 has to be sufficiently small, and thus, the wave components in ϕ are also quite small. This implies that *scalar-type gravitational waves*, which are directly related to ϕ, are negligible in this theory, although *scalar waves* associated with φ are emitted to carry energy and angular momentum from the system.

C. Equations of state employed

In this paper, we employ APR4 [38] and H4 [39] EOSs as in Refs. [27, 36]. We remind that the APR4 EOS was derived by a variational method with modern nuclear potentials for the hypothetical components composed of neutrons, protons, electrons, and muons. The H4 EOS was derived by a relativistic mean-field theory including effects of hyperons. Here, for both EOSs, the maximum allowed mass of spherical neutron stars is larger than $2M_\odot$ ($\approx 2.20M_\odot$ for APR4 and $\approx 2.03M_\odot$ for H4), and hence, the observational constraints by the latest discovery of two-solar mass neutron stars [25, 40] are satisfied for these EOSs. The main difference between the two EOSs is that APR4 is a stiff but relatively soft EOS in which the stellar radius of a spherical neutron star with canonical mass $1.35M_\odot$ is ≈ 11 km while H4 is a relatively stiff EOS in which the stellar radius of a spherical neutron star with canonical mass $1.35M_\odot$ is ≈ 13.5 km. This stiffness is quite important for determining the properties of the scalarized neutron stars, as we shall describe in Sec. III.

D. Initial conditions for quasiequilibrium configurations

We now explain how we prepare the initial conditions of the numerical simulations using quasiequilibrium configurations for a binary in a circular orbit with angular velocity Ω. To derive quasiequilibrium configurations, we adopt the conformal flatness formulation, that is

$$\gamma_{ij} = \psi^4 f_{ij}, \tag{25}$$

we assume the presence of a helical Killing vector, $(\partial_t + \Omega\partial_\varphi)^a$, and the maximal slicing $K = 0$ [41]. Here, f_{ij} is the flat spatial metric. For the fluid part, the equations are the same as those in Einstein's gravity in the Jordan frame. Thus, assuming that the velocity field is irrotational, the first integral of the hydrodynamics equations is readily determined in the same manner as those in Einstein's gravity [42].

The basic equations for the tensor field are obtained from the Hamiltonian and momentum constraints, together with Eq. (8) under the condition $K = 0$. Except for the modifications introduced by the presence of the scalar field ϕ, the equations are the same as that in Einstein's gravity. The Hamiltonian and momentum constraints are, respectively, written as

$$\begin{aligned}\overset{(0)}{\Delta}\psi = &-2\pi\phi^{-1}\rho_{\rm h}\psi^5 - \frac{1}{8}\tilde{A}_{ij}\tilde{A}^{ij}\psi^5 \\ &-\frac{\psi^5}{8}\left[\omega\phi^{-2}\{\Pi^2 + (D_i\phi)D^i\phi\} + 2\phi^{-1}D_iD^i\phi\right],\end{aligned} \tag{26}$$

and

$$\begin{aligned}\overset{(0)}{D}_i(\psi^6\tilde{A}^i{}_j) = \psi^6\Big[&8\pi\phi^{-1}J_j + \omega\phi^{-2}\Pi\overset{(0)}{D}_j\phi \\ &+\phi^{-1}(\overset{(0)}{D}_j\Pi - \tilde{A}^i{}_j\overset{(0)}{D}_i\phi)\Big],\end{aligned} \tag{27}$$

where $\overset{(0)}{\Delta}$ and $\overset{(0)}{D}_i$ are the Laplacian and covariant derivative with respect to f_{ij}. $\tilde{A}_{ij}$ is the tracefree conformal extrinsic curvature satisfying $K_i{}^j = \tilde{A}_i{}^j$ for $K = 0$ and its equation is derived from the evolution equation for γ_{ij} with Eq. (25) as

$$\tilde{A}_{ij} = \frac{1}{2\alpha}\left(\overset{(0)}{f_{ik}D_j}\beta^k + \overset{(0)}{f_{jk}D_i}\beta^k - \frac{2}{3}f_{ij}\overset{(0)}{D_k}\beta^k\right), \tag{28}$$

where indices of $\tilde{A}_{ij}$, $\tilde{A}^{ij}$, and $\overset{(0)}{D}_i$ are raised and lowered by f^{ij} and f_{ij}. The condition $K=0$ yields

$$\overset{(0)}{\Delta}\chi = \chi\psi^4\Bigg[2\pi\phi^{-1}(2S+\rho_{\rm h}) + \frac{7}{8}\tilde{A}_{ij}\tilde{A}^{ij} + \frac{1}{8}\omega\phi^{-2}\left\{7\Pi^2 - (D_i\phi)D^i\phi\right\} + \frac{3}{4\phi}\Bigg\{D_iD^i\phi - \frac{2}{(2\omega+3)} \times \left(8\pi T + \frac{d\omega}{d\phi}(\Pi^2 - (D_k\phi)D^k\phi)\right)\Bigg\}\Bigg], \quad (29)$$

where $\chi := \alpha\psi$. Note that we will replace the Laplacian term of $D_iD^i\phi$ using the equation for ϕ (see below).

In addition to these equations, we have to solve the equation for φ. If we simply impose that φ satisfies the helical symmetry, we have

$$\Phi = -\alpha^{-1}(\Omega\partial_\varphi + \beta^i\partial_i)\varphi. \quad (30)$$

In this case, $D_i\phi$ and Π in Eq. (11) behave as $\propto r^{-1}$ in the far zone. If so, the spacetime cannot be asymptotically flat because in the Hamiltonian constraint there exist terms in the right-hand side that are proportional to Π^2 and $(D_i\phi)D^i\phi$. Thus Π and $D_i\phi$ have to be of order r^{-2} in the far zone. To guarantee this condition, we simply set $\Pi=0$. Then, Eq. (11) becomes an elliptic-type equation so that $D_i\phi = O(r^{-2})$ is guaranteed in the far-zone. The boundary condition to be imposed for φ is $\varphi\to\varphi_0$ for $r\to\infty$. Note that the resulting elliptic equation for φ can be substituted in the right-hand side of Eq. (5).

We compute the quasiequilibrium configurations using a new code which is developed from a general-relativistic code originally implemented in the spectral-method library LORENE [43]. We shall present details of the numerical study of quasiequilibrium configurations in Ref. [23].

E. Definition of masses

In scalar-tensor theories of gravity there are several definitions of masses. Here, we review them briefly.

The ADM mass is defined as

$$M_{\rm ADM} := \frac{1}{16\pi}\oint_\infty \gamma^{jk}\gamma^{jl}(\partial_k\gamma_{ij} - \partial_i\gamma_{jk})\overset{(0)}{dS}_l, \quad (31)$$

where $\overset{(0)}{dS}_l$ is the surface integral operator in flat space and $\oint_\infty$ denotes $\oint_{r\to\infty}$. In the conformally flat spatial hypersurface, the ADM mass may be defined as

$$M_{\rm ADM} := -\frac{1}{2\pi}\oint_\infty Q\gamma^{jk}\partial_k\psi\overset{(0)}{dS}_j, \quad (32)$$

where Q is a function which reduces to unity when $r\to\infty$.

From the asymptotic behavior of ϕ at $r\to\infty$, we can define the scalar mass $M_{\rm S}$ [8, 45] as

$$\phi = \phi_0 + \frac{2M_{\rm S}}{r} + \mathscr{O}\left(\frac{1}{r^2}\right), \quad (33)$$

where $\phi_0(=\exp(\varphi_0^2/2))$ is a constant close to unity because $\varphi_0 \ll 1$ (see Sec. III). Equation (33) implies that the asymptotic behavior of φ is

$$\varphi = \varphi_0 + \frac{M_\varphi}{r} + \mathscr{O}\left(\frac{1}{r^2}\right), \quad (34)$$

where M_φ is constant and related to $M_{\rm S}$ by $2M_{\rm S}/\varphi_0$. In presence of a timelike Killing vector or helical Killing vector, we can define the Komar mass [46], which is related to the ADM mass and the scalar mass by [47]

$$M_{\rm K} = M_{\rm ADM} + 2M_{\rm S}. \quad (35)$$

In addition, it is useful to define the tensor mass [45]

$$M_{\rm T} = M_{\rm ADM} + M_{\rm S}, \quad (36)$$

which, as Lee showed in Ref. [45], obeys a conservation law similar to the one that the ADM mass obeys in general relativity. Thus, in scalar-tensor theories of gravity, we find it more appropriate to identify the neutron-star mass with the tensor mass rather than the ADM mass. Henceforth, we shall use this identification and set the neutron-star mass $M_{\rm NS} := M_{\rm T}$.

F. Simulation set-up and validation

We perform numerical simulations using an adaptive-mesh refinement code `SACRA-ST` that was implemented by modifying the original code for general relativity [33]. As done for the simulations in Refs. [27, 36], the semi-major diameter of neutron stars is initially covered by ≈ 100 grid points (we refer to this grid resolution as high resolution). For APR4 and H4, the finest grid resolution is ≈ 0.17 and 0.22 km, respectively. We also perform lower-resolution simulations covering the semimajor diameter by ≈ 67 and 80 grid points (we refer to these grid resolutions as low and medium resolutions), and check that we achieve sufficient convergence to trust the conclusions of this paper (see Appendix B for details).

We also confirm the validity of our code by performing (i) simulations of spherical stars, (ii) longterm evolutions of scalarized spherical neutron stars, and (iii) collapses of a scalarized neutron star to a black hole. The success of these tests give us confidence in our new scalar-tensor code (see Appendix A for details).

III. PARAMETERS CHOICE FOR SPONTANEOUS SCALARIZATION IN BINARY NEUTRON STARS

In this section, we first review the key mechanism responsible for spontaneous scalarization in a single star and then present a physical argument to explain why scalarization can occur in binary systems even if the scalar charge at large separations were very small. Furthermore, for the EOSs employed in this paper, we determine the values of B and φ_0 such that they satisfy the constraints imposed by pulsar-timing observations [24, 25]. We shall perform numerical simulations for those choices of the parameters.

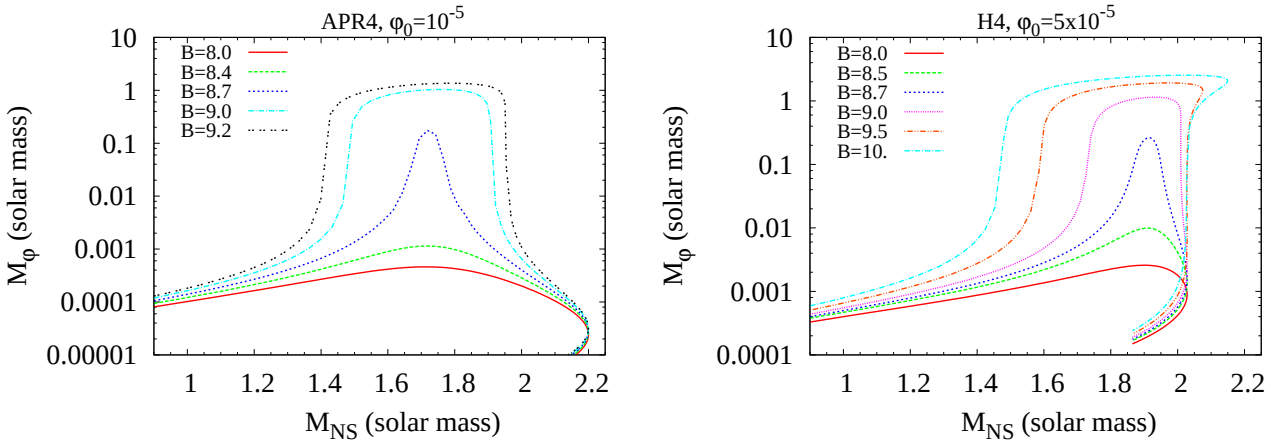

FIG. 1. We plot the value of M_φ as a function of the neutron-star mass for spherical, isolated neutron stars using the APR4 and H4 EOSs, and several values of B. The values of φ_0 are chosen to be 10^{-5} and 5×10^{-5} for APR4 and H4 EOSs, respectively.

A. Spontaneous scalarization in an isolated star

Here, we follow Ref. [11] and review the key idea underlying spontaneous scalarization. For simplicity we restrict the discussion to the static case and we neglect the gravitational field and nonlinear terms in φ. Within these approximations Eq. (22) can be written as

$$\Delta\varphi = 2\pi BT\varphi, \tag{37}$$

where Δ denotes the flat Laplacian. Assuming that relativistic corrections are small, we have $T\approx-\rho<0$. We also assume that $T=$ const., $B>0$, and set $k^2=-BT$. Considering that the star is spherically symmetric in isolation, we find that the solution of Eq. (37) is [11]

$$\varphi = \begin{cases} \mathscr{A}\dfrac{\sin(kr)}{r} & r\le R, \\ \dfrac{M_\varphi}{r}+\varphi_0 & r\ge R, \end{cases} \tag{38}$$

where $\mathscr{A}$ is a constant and R denotes the stellar radius. The continuity conditions of φ and $d\varphi/dr$ at $r=R$ then yield

$$\mathscr{A} = \frac{\varphi_0}{k\cos(kR)}, \tag{39}$$

$$M_\varphi = \varphi_0[k^{-1}\tan(kR)-R], \tag{40}$$

This suggests that for $kR\to\pi/2$, φ, as well as M_φ, significantly increases, i.e., the scalarization occurs, irrespective of the value of φ_0. Thus, the onset of scalarization depends on three parameters, B, T, and R. Then, if we assume $T\sim-\rho$ and use $\rho R^3\sim M_{\rm NS}$ where $M_{\rm NS}$ is the mass of the neutron star, we have that kR is proportional to $B^{1/2}(M_{\rm NS}/R)^{1/2}$. Thus we conclude that the scalarization is determined by two parameters: B and the stellar compactness (or the mass of the neutron star).

For $B<0$ or $T>0$ (i.e., for $BT>0$), the solution of Eq. (37) in spherical symmetry is [11]

$$\varphi = \begin{cases} \mathscr{A}\dfrac{\sinh(kr)}{r} & r\le R, \\ \dfrac{M_\varphi}{r}+\varphi_0 & r\ge R, \end{cases} \tag{41}$$

and the continuity conditions yield

$$\mathscr{A} = \frac{\varphi_0}{k\cosh(kR)}, \tag{42}$$

$$M_\varphi = \varphi_0[k^{-1}\tanh(kR)-R]. \tag{43}$$

Here we set $k^2=BT$. Thus, in this case, the scalarization is not likely to occur for any value of B, T, and R. This suggests that for the ultra-relativistic case with $T=-\rho h+4P>0$ (and $B>0$), the scalarization does not occur.

The above analysis suggests that when the scalarization *does not* occur, M_φ is proportional to φ_0 and we can write

$$M_\varphi = F(M_{\rm NS},B)\varphi_0, \tag{44}$$

where F is a function that depends on $M_{\rm NS}$ and B. From a numerical analysis of spherical neutron stars in equilibrium, we indeed find that this relation is satisfied as long as the spontaneous scalarization does not set in.

In Fig. 1 we plot M_φ as a function of the neutron-star mass $M_{\rm NS}$ for the APR4 and H4 EOSs, using $\varphi_0=10^{-5}$ and $=5\times10^{-5}$, respectively. We observe the following interesting properties. If $M_{\rm NS}$ is smaller than a critical value $M_{\rm NSc1}$, M_φ is much smaller than $M_{\rm NS}$. The critical value depends strongly on the value of B. For larger values of B, $M_{\rm NSc1}$ is smaller, and hence, spontaneous scalarization sets in for smaller neutron-star masses. By contrast, if $M_{\rm NS}$ is larger than a critical value $M_{\rm NSc2}$, M_φ is again much smaller than $M_{\rm NS}$. Thus, when neutron stars have sufficiently large masses spontaneous scalarization never sets in. This is due to the fact that for those large masses, the relativistic effects are so significant that $T=-\rho h+4P$ could be positive. This would imply that observations of neutron stars with large masses, e.g., $\approx 2M_\odot$, may not be very useful in constraining the value of B. Finally,

TABLE I. The value of F for the APR4 EOS with $\varphi_0 = 10^{-5}$ and the H4 EOSs with $\varphi_0 = 5\times10^{-5}$. The unit of F is $M_\odot$. When "—" appears, it means that for such a model, the relation (44) breaks down, thus scalarization occurs.

APR4	B				
$M_{\rm NS}(M_\odot)$	8.0	8.5	9.0	9.5	10.0
1.30	21	32	62	3.8×10^2	—
1.35	24	39	91	—	—
1.40	27	48	1.6×10^2	—	—
1.45	30	59	4.0×10^2	—	—
1.50	34	75	—	—	—

H4	B				
$M_{\rm NS}(M_\odot)$	8.0	8.5	9.0	9.5	10.0
1.30	14	18	24	34	54
1.35	16	21	28	42	77
1.40	17	23	34	55	1.3×10^2
1.45	19	27	41	77	3.7×10^2
1.50	22	31	51	1.2×10^2	—

for $M_{\rm NSc1} < M_{\rm NS} < M_{\rm NSc2}$, neutron stars are spontaneously scalarized, for certain values of B, e.g., $B \gtrsim 8.5$ for the APR4 EOS. Indeed, in these cases, M_φ is on the order of $M_{\rm NS}$. Using the qualitative analysis worked out at the beginning of this section, in particular Eq. (40), we find that the value of M_φ could diverge when spontaneous scalarization occurs. However, when using the realistic *nonlinear* equation for φ, instead of Eq. (37), we find that nonlinear effects always constrain M_φ to be at most equal to the neutron-star mass $M_{\rm NS}$.

B. Condition for scalarization in inspiraling binary neutron stars

As described in the previous section, for an isolated, spherical neutron star in which the scalarization has not occurred, the profile of φ is approximately described by Eq. (34), where $M_\varphi \ll M_{\rm NS}$. Given this field configuration, we now suppose that the neutron star is in a binary system and it is not yet spontaneously scalarized. In this case it is natural to assume that Eq. (44) gets approximately modified by the companion star as

$$M_\varphi \approx F(M_{\rm NS},B)\left(\varphi_0 + \frac{M_\varphi}{a}\right), \tag{45}$$

where a is the orbital separation. Namely, the value of φ just outside the neutron star is enhanced by the presence of the companion. (Note that for simplicity we are considering an equal-mass (or nearly equal-mass) binary.) Solving Eq. (45) for M_φ yields

$$M_\varphi \approx F(M_{\rm NS},B)\varphi_0\left(1 - \frac{F(M_{\rm NS},B)}{a}\right)^{-1}, \tag{46}$$

and hence, M_φ can increase steeply and can become on the order of $M_{\rm NS}$ when $a \sim F(M_{\rm NS},B)$. Thus, even if the values of φ_0 and B are such that spontaneous scalarization of the isolated neutron star is absent or it occurs only weakly, the neutron star can be strongly scalarized if it is part of a binary system and if the condition $a \lesssim F(M_{\rm NS},B)$ is satisfied. Because this scalarization sets in when the neutron star is part of a binary system, we denote it *dynamical* scalarization to distinguish it from spontaneous scalarization. [2] This property is indeed confirmed in our accompanying paper [23]. Let us now investigate when the condition $a \lesssim F(M_{\rm NS},B)$ holds.

We list in Table I the values of F for different neutron-star masses and different values of B, for the two EOSs that we use in this paper, notably APR4 and H4. (When "—" appears, it means that for such a model the spontaneous scalarization does occur, and thus, Eq. (44) no longer holds.) For binary neutron stars, the merger occurs typically at $a = 30-45$ km $\approx 20-30M_\odot$ depending on the EOS. This implies that if F is smaller than $20-30M_\odot$, dynamical scalarization does not occur during the inspiral stage. We find that for dynamical scalarization to occur, F has to be larger than at least $20M_\odot$ for APR4 and $\sim 25M_\odot$ for H4. As we see in Table I, for $M_{\rm NS} = 1.35M_\odot$, dynamical scalarization can always set in before merger for APR4 EOS when $B \gtrsim 8.0$. By contrast, for H4 EOS, dynamical scalarization can take place only when $B \gtrsim 9.0$ for $M_{\rm NS} = 1.35M_\odot$. These properties are confirmed in our accompanying paper [23].

Before ending this section, we present the analysis for unequal-mass binary systems. Let $M_{\varphi,1}$ and $M_{\varphi,2}$ be the values of M_φ for stars 1 and 2. Then, Eq. (45) can be rewritten in two equations

$$M_{\varphi,1} \approx F_1\left(\varphi_0 + \frac{M_{\varphi,2}}{a}\right), \tag{47}$$

$$M_{\varphi,2} \approx F_2\left(\varphi_0 + \frac{M_{\varphi,1}}{a}\right), \tag{48}$$

where $F_1 := F(M_{\rm NS,1},B)$ and $F_2 := F(M_{\rm NS,2},B)$ with $M_{{\rm NS},i}$ being the mass of neutron star i. Equations (47) and (48) yield

$$M_{\varphi,1} \approx \varphi_0 F_1\left(1+\frac{F_2}{a}\right)\left(1-\frac{F_1F_2}{a^2}\right)^{-1}, \tag{49}$$

$$M_{\varphi,2} \approx \varphi_0 F_2\left(1+\frac{F_1}{a}\right)\left(1-\frac{F_1F_2}{a^2}\right)^{-1}. \tag{50}$$

Thus, we expect the scalarization to occur when $a \approx \sqrt{F_1F_2}$ for both neutron stars approximately simultaneously.

[2] We note that Ref. [21] simulated a binary configuration in which neutron stars are not initially spontaneously scalarized and found that *induced* scalarization can set in in the late inspiral. They also gave a qualitative explanation of this phenomenon resorting to energetically favoured arguments discussed in Ref. [44].

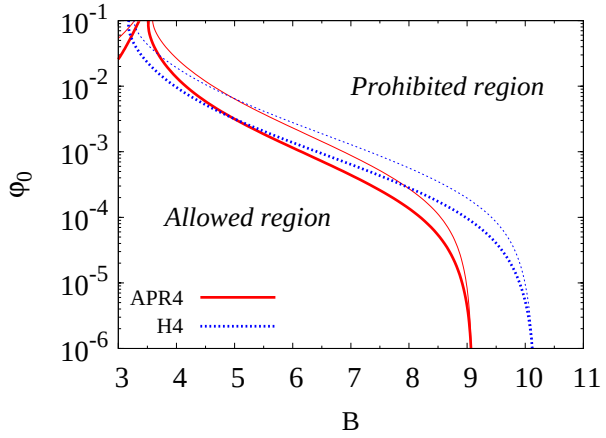

FIG. 2. The allowed region in the B-φ_0 plane derived from the constraint equation (57) setting the pulsar mass to $1.46M_\odot$ for PSR J1738+0333. The thick and thin solid curves show the result for $\alpha_r = 0.05$ and 0.2, respectively. At $B \approx 3.5$ for the APR4 EOS and $B \approx 3.2$ for the H4 EOS, the dipole radiation is suppressed because the relation $M_\varphi/M_{\rm NS} \approx M_{\varphi,{\rm WD}}/M_{\rm WD}$ is satisfied [12, 24]. Note that the constraint by the Cassini spacecraft [10] is written as $B\varphi_0^2 \lesssim 5\times10^{-5}$ and is stronger than that imposed by the binary pulsar for $B \lesssim 5$.

C. Constraints from pulsar binary systems

Pulsar timing observations of binary systems composed of a neutron star and a white dwarf [24, 25] impose the strongest constraints on B and φ_0 for a high value of $B \gtrsim 5$. The constraints come primarily from the fact that the scalar-wave luminosity has to be substantially smaller than the gravitational-wave luminosity.

The neutron-star masses measured in Refs. [24, 25] are $M_{\rm NS} = 1.46^{+0.06}_{-0.05}M_\odot$ and $M_{\rm NS} = 2.01 \pm 0.04 M_\odot$ at one–σ error, respectively. As we shall find below, those observations imply that neutron stars with masses $\lesssim 1.46M_\odot$ and $\gtrsim 2.01M_\odot$ cannot be scalarized and that the possible values of B, which depend on the EOS, are strongly limited. Although Refs. [24, 25] has already constrained the DEF scalar-tensor model, they did it employing one specific EOS for the nuclear matter [13]. As we have emphasized when discussing Fig. 1, the constraint on B depends on the EOS. Therefore, our analysis, although similar to and simpler than the one of Refs. [24, 25], pays special attention to the dependence of the constraints on the EOS.

In the following we work at leading order, that is we neglect all higher-order, nonlinear corrections in the luminosity (see Refs. [13, 19, 48] for more precise results). The gravitational-wave luminosity from the tensor quadrupole moment in a binary system in circular orbits is

$$\left.\frac{dE}{dt}\right|_{\rm tensor\ quad} = \frac{32}{5}\left(\frac{\mu}{m}\right)^2\left(\frac{m}{a}\right)^5, \tag{51}$$

where m, μ, and a are the total mass, the reduced mass $M_{\rm WD}M_{\rm NS}/m$, and the orbital separation, respectively. Hereafter, we consider binaries composed of a neutron star of mass $M_{\rm NS}$ and a white dwarf of mass $M_{\rm WD}$. We derive the scalar-wave luminosity from the scalar dipole moment integrating Eq. (22). The relevant term in the wave zone is $\varphi \to \dot{d}_i n^i/r$ where n^i is the unit spatial vector pointing along the radial direction and d_i is the scalar dipole moment with magnitude

$$\frac{a}{m}\left|M_{\rm WD}M_\varphi - M_{\rm NS}M_{\varphi,{\rm WD}}\right| = a\mu\left|\frac{M_\varphi}{M_{\rm NS}} - \frac{M_{\varphi,{\rm WD}}}{M_{\rm WD}}\right|. \tag{52}$$

Here, M_φ and $M_{\varphi,{\rm WD}}$ are the scalar charges of the neutron star and white dwarfs, and $\dot{d}_i = (d/dt)d_i$. Substituting this dipole-moment contribution into the stress-energy tensor of the scalar field, we find that the scalar-wave luminosity from the scalar dipole moment in a neutron star-white dwarf binary in a circular orbit is

$$\left.\frac{dE}{dt}\right|_{\rm scalar\ dip} = \frac{1}{6}\left(\frac{2}{B} - \frac{1}{2}\varphi_0^2\right)\left(\frac{\mu}{m}\right)^2\left(\frac{m}{a}\right)^4 \times\left(\frac{M_\varphi}{M_{\rm NS}} - \frac{M_{\varphi,{\rm WD}}}{M_{\rm WD}}\right)^2. \tag{53}$$

Assuming that $B\varphi_0^2 \ll 1$, we write $2/B - \varphi_0^2/2 \approx 2/B \approx \omega_0\varphi_0^2$ where ω_0 denotes the asymptotic value of ω, which has to be $\gtrsim 4\times10^4$ [10]. Thus in the following, we neglect the term $\varphi_0^2/2$ in Eq. (53). The ratio of the luminosities (51) and (53) is

$$\alpha_r := \frac{(dE/dt)_{\rm scalar\ dip}}{(dE/dt)_{\rm tensor\ quad}} = \frac{5}{96B}\left(\frac{M_\varphi}{M_{\rm NS}} - \frac{M_{\varphi,{\rm WD}}}{M_{\rm WD}}\right)^2\left(\frac{a}{m}\right). \tag{54}$$

If observations constrain α_r to a certain value, then, the following constraint on M_φ holds

$$M_\varphi < \left(\sqrt{\frac{96B\alpha_r}{5}}\left(\frac{m}{a}\right)^{1/2} + \frac{M_{\varphi,{\rm WD}}}{M_{\rm WD}}\right)M_{\rm NS}, \tag{55}$$

for $M_\varphi/M_{\rm NS} > M_{\varphi,{\rm WD}}/M_{\rm WD}$ and

$$M_\varphi > \left(-\sqrt{\frac{96B\alpha_r}{5}}\left(\frac{m}{a}\right)^{1/2} + \frac{M_{\varphi,{\rm WD}}}{M_{\rm WD}}\right)M_{\rm NS}, \tag{56}$$

for $M_\varphi/M_{\rm NS} < M_{\varphi,{\rm WD}}/M_{\rm WD}$. We notice that for large values of $B \gtrsim 4$, $M_\varphi/M_{\rm NS} > M_{\varphi,{\rm WD}}/M_{\rm WD}$.

Currently, the strongest constraint on the DEF scalar-tensor theory [11–13] is due to the observation of the white dwarf-neutron star PSR J1738+0333 system [24]. For this system, $M_{\rm NS} = 1.46^{+0.06}_{-0.05}M_\odot$, $m = 1.65^{+0.07}_{-0.06}M_\odot$, and the orbital period is 0.35479 days with ≈ 0 eccentricity. These data imply $\sqrt{m/a} = (1.19\pm0.02)\times10^{-3}$. For this binary system, the decrease rate of the orbital period is measured with $\approx 12\%$ error and agrees with the prediction of general relativity within $\sim 7\%$ at the one–σ level. This would imply that in this binary system the scalar-wave luminosity cannot exceed $\sim 5\%$ of the gravitational-wave luminosity, i.e., $\alpha_r \lesssim 0.05$. The same qualitative conclusion would apply for the PSR J0348+0432 binary [25], which contains a neutron star with mass $\sim 2M_\odot$.

The numerical calculation shows that $M_{\varphi,{\rm WD}}/M_{\rm WD} \approx B\varphi_0/2$ for low-mass white dwarfs with $M_{\rm WD} \lesssim 0.2M_\odot$. This

relation is also expected from Eq. (37) with $T \approx -\rho$ which holds in the Newtonian limit. Thus, we employ this relation in the following.

Then, for PSR J1738+0333, we can write Eq. (55) as

$$M_\varphi < \left[5.1\times10^{-3}M_\odot\left(\frac{\alpha_r}{0.05}\right)^{1/2}\left(\frac{B}{9}\right)^{1/2}\left(\frac{\sqrt{m/a}}{1.19\times10^{-3}}\right) + 6.57M_\odot\left(\frac{B}{9}\right)\varphi_0\right]\left(\frac{M_{\rm NS}}{1.46M_\odot}\right). \quad (57)$$

Equation (56) is also written in the similar form. Using these constraint relations for PSR J1738+0333 , we can determine the allowed regions in the parameter space B–φ_0 of the scalar-tensor model. We do it constructing spherical-star configurations with $M_{\rm NS} = 1.46M_\odot$ and different values of B and φ_0. In Fig. 2 we show those allowed regions for a spherical neutron star of mass $1.46M_\odot$. We find that B has to be smaller than ≈ 9.0 and 10.0 for APR4 and H4 EOSs irrespective of the value of φ_0. Therefore, $M_\varphi \ll M_{\rm NS}$ and the PSR J1738+0333 binary pulsar is not scalarized at the separation at which it has been observed. The allowed regions vary if we take into account the one-σ error for the mass of the pulsar. For example, if the mass of the pulsar were $\approx 1.40M_\odot$, the constraint is less severe (allowed region is slightly wider), whereas if it were $\approx 1.50M_\odot$, the constraint is more severe.

It is straightforward to derive a constraint similar to Eq. (57) for the PSR J0348+432 binary pulsar. Also in this case we find that M_φ has to be much smaller than $M_{\rm NS} \sim 2.0M_\odot$. As a consequence, also the PSR J0348+432 binary pulsar is not scalarized at the binary separation at which it is observed. However, as it can be seen in Fig. 1, for APR4 EOS, the constraint (57) is not as strong as the one we obtain for PSR J1738+0333, because this pulsar has a large mass, so the relativistic effects are in any case too significant to induce the scalarization (we note that this is also the case for relatively soft EOSs in which the radius of $1.35M_\odot$ neutron stars is 11 – 12 km). For H4 EOS, we find that the value of B has to be smaller than ~ 9.0 and in this case, neutron stars are scalarized up to $M_{\rm NS} \sim 2M_\odot$.

Thus to summarize, because of the constraints coming from the observations of PSR J1738+0333 and PSR J0348+0432, B has to be smaller than ~ 9.0, both for APR4 and H4 EOSs. We note that for stiff EOSs in which the radius of neutron stars is large ~ 15 km and the maximum mass for spherical neutron stars is larger than $2.5M_\odot$, the constraint imposed by the observation of PSR J0348+0432 is quite severe. For example, for MS1 EOS [49] in which the radius of $1.35M_\odot$ neutron stars is ≈ 14.5 km, B has to be smaller than ~ 8.8.

Finally, because the PSR J1738+0333 binary pulsar is not scalarized, we can use Eq. (44) to rewrite Eq. (55) as

$$\varphi_0 < 5.1\times10^{-5}\left(\frac{\alpha_r}{0.05}\right)^{1/2}\left(\frac{B}{9}\right)^{1/2}\left(\frac{M_{\rm NS}}{1.46M_\odot}\right) \times\left(\frac{F - BM_{\rm NS}/2}{100M_\odot}\right)^{-1}\left(\frac{\sqrt{m/a}}{1.19\times10^{-3}}\right). \quad (58)$$

The above equation implies that φ_0 is smaller than $\sim 10^{-5}$ and $\sim 10^{-4}$ for APR4 and H4 EOSs with $M_{\rm NS} = 1.46M_\odot$, $\alpha_r = 0.05$, and $B = 9.0$, because for this mass, $F \sim 500M_\odot$ and $\sim 50M_\odot$, respectively. Thus, $\omega_0 \approx 2/(B\varphi_0^2)$ has to be larger than $\sim 2\times10^9$ and $\sim 2\times10^7$ for APR4 and H4, respectively, if B is as large as ~ 9 – 10. These constraints are much stronger than those given in Ref. [10], as also found in Ref. [24].

In the previous section, we have found that for $M_{\rm NS} = 1.35M_\odot$, the condition for the onset of dynamical scalarization during the inspiral with the APR4 EOS is relatively weak, $B \gtrsim 8.0$. By contrast, with the H4 EOS, the condition for dynamical scalarization is rather limited as $B \gtrsim 9.0$. Combining the constraints derived in this section, we obtain the following conditions for the onset of dynamical scalarization during the inspiral stage: for the APR4 EOS, $8 \lesssim B \lesssim 9$, while for the H4 EOS, we find only a very narrow window in the vicinity of $B \sim 9.0$. These analyses clearly illustrate that the EOS of neutron stars is a key ingredient to determine the onset of dynamical scalarization in the inspiral stage.

D. Choice of scalar-tensor parameters

Taking into account the constraints of the previous section, we employ the following values of B in the numerical simulations: $B = 9.0$, 8.7, 8.4, 8.0, and 7.5 for the APR4 EOS, and 9.5, 9.0, 8.5, and 8.0 for the H4 EOS. The value of $B = 9.5$ for the H4 EOS is not allowed by the pulsar-timing observations as mentioned above. However, we shall investigate this case because we want to show that scalarization in binary neutron stars occurs qualitatively in a universal manner irrespective of the EOS employed. For small values of $B \lesssim 8.0$ for APR4 and $\lesssim 9.0$ for H4, we do not expect dynamical scalarization to occur during the inspiral stage. However, the scalarization can still occur in the *merger stage*. This is why we employ such a small value for B.

For a given value of B, the value of φ_0 is also constrained (see Sec. III C). Taking into account the constraint given by Eq. (58), we choose $\varphi_0 = 10^{-5}$ for the APR4 EOS and 5×10^{-5} for the H4 EOS. Note that the results presented in this paper depend very weakly on the choice of φ_0.

For the chosen values of B with neutron-star mass $\approx 1.35M_\odot$, dynamical scalarization of neutron stars in a binary system occurs for $a \lesssim 100M_\odot \approx 150$ km. For the total mass of $2.7M_\odot$, this implies that dynamical scalarization can occur only for $f \gtrsim 100$ Hz where f is the gravitational-wave frequency. Therefore, due to the presence of the strong constraints from the observations of PSR J1738+0333 [24] and PSR J0348+0432 [25], if neutron stars have canonical masses 1.3 – $1.4M_\odot$, the scalarization can take place only if the neutron star is in a compact binary system.

In this paper we choose the initial value of the angular velocity as $m\Omega = 0.026$ for the APR4 EOS and 0.023 for the H4 EOS with $m = 2.7M_\odot$; the initial orbital period is 3.21 ms and 3.63 ms, respectively; the initial separation is $a/m \approx (m\Omega)^{-2/3} = 11.4$ for the APR4 EOS and 12.4 for the H4 EOS; $a \approx 31M_\odot$ for the APR4 EOS and $33M_\odot$ for the H4 EOS. Thus, for $B = 9.0$, 8.7, and 8.4 with the APR4 EOS and for $B = 9.5$ with the H4 EOS, for which $a < F$, dynamical scalarization has already occurred at the initial separation (see

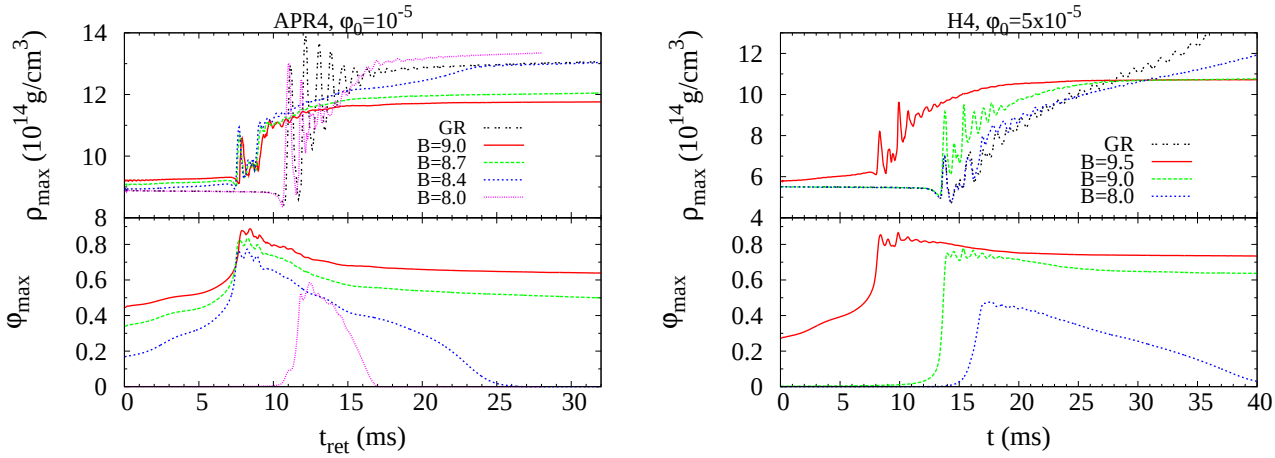

FIG. 3. Evolution of the maximum values of the rest-mass density and scalar field φ for several models of $m = 2.7M_\odot$ with the APR4 EOS (left panel) and the H4 EOS (right panel). The merger sets in at the time where the maximum density steeply increases. We note that for $B \geq 8.4$ with APR4 EOS and for $B = 9.5$ with H4 EOS, the scalarization already occurred at $t = 0$ (cf. Table II).

TABLE II. We list key quantities of our numerical simulations: EOS, the value of B, initial angular velocity in units of m^{-1}, and total number of orbits. The total mass of the binary neutron stars is $2.7M_\odot$. In the last column, we indicate when the scalarization occurs. We consider that dynamical scalarization has occurred when the value of M_φ computed for a neutron-star in a binary cannot be described by Eq. (44) (see Ref. [23] for details).

EOS	B	$m\Omega$	Orbits	Scalarization
APR4	GR	0.026	≈ 5.0	—
APR4	7.5	0.026	≈ 5.0	no scalarization
APR4	8.0	0.026	≈ 5.0	at merger
APR4	8.4	0.026	≈ 3.5	$m\Omega \approx 0.024$
APR4	8.7	0.026	≈ 3.5	$m\Omega \approx 0.014$
APR4	9.0	0.026	≈ 3.5	$m\Omega \approx 0.005$
H4	GR	0.023	≈ 5.0	—
H4	8.0	0.023	≈ 5.0	after merger
H4	8.5	0.023	≈ 5.0	after merger
H4	9.0	0.023	≈ 5.0	at merger
H4	9.5	0.023	≈ 3.0	$m\Omega \approx 0.017$

Table II). On the other hand, for $B \leq 8.0$ with the APR4 EOS and for $B \leq 9.0$ with the H4 EOS, dynamical scalarization has not yet occurred at the initial separation because $a > F$.

IV. NUMERICAL RESULTS

A. Characteristics of the merger process

In Fig. 3 we plot the maximum values of the neutron-star density ρ and scalar field φ as functions of the time for several values of B and for the APR4 EOS (left panel) and the H4 EOS (right panel) (see also Appendix B for a convergence study). For comparison, we also plot the maximum density for the general-relativistic case. Note that the merger sets in at the time where the maximum density steeply increases. We observe the following features of the merger process:

- For $B \leq 8.0$ with the APR4 EOS and for $B \leq 9.0$ with the H4 EOS, the maximum value of φ, $\varphi_{\rm max}$, is always much smaller than unity before the onset of the merger. This shows that for these models, the scalarization does not occur during the inspiral stage as we expected in the analysis of Sec. III.

- Even for the initially weakly scalarized case (e.g., $B = 8.4$ with the APR4 EOS), the scalar fields are amplified as the orbital separation decreases, signaling the occurrence of dynamical scalarization.

- For the binary neutron stars that have scalarized, the duration of the inspiral stage is much shorter than that for the nonscalarized case [21]. For both EOSs, we find that starting from the same initial frequency $m\Omega$, the inspiral stage of the scalarized binaries is shorter than the one of binaries in general relativity by $1-2$ orbits. In the general-relativistic case the inspiral stage lasts for ≈ 5 orbits for both APR4 and H4 EOSs (cf. Table II). Thus, the scalarization shortens the inspiral stage by a significant fraction. The reason for the modification of the inspiral orbits for the scalarized case is that the increase rate of the absolute value of the binding energy is *decreased* by the scalarization effect. We have also investigated this effect using quasiequilibrium sequences of binary neutron stars in Ref. [23]. We notice that in the scalarized stage, the orbital motion does not depend much on the values of B.

- For the binary neutron stars that undergo dynamical scalarization (i.e., they have scalarized because of the presence of the companion), the maximum density *increases* with the decrease of the orbital separation. This is in contrast with the general-relativistic case in which the maximum density decreases with the decrease of the orbital separation because of the tidal force exerted by the companion star. The continuous increase of the maximum density in the scalarized case is due to the

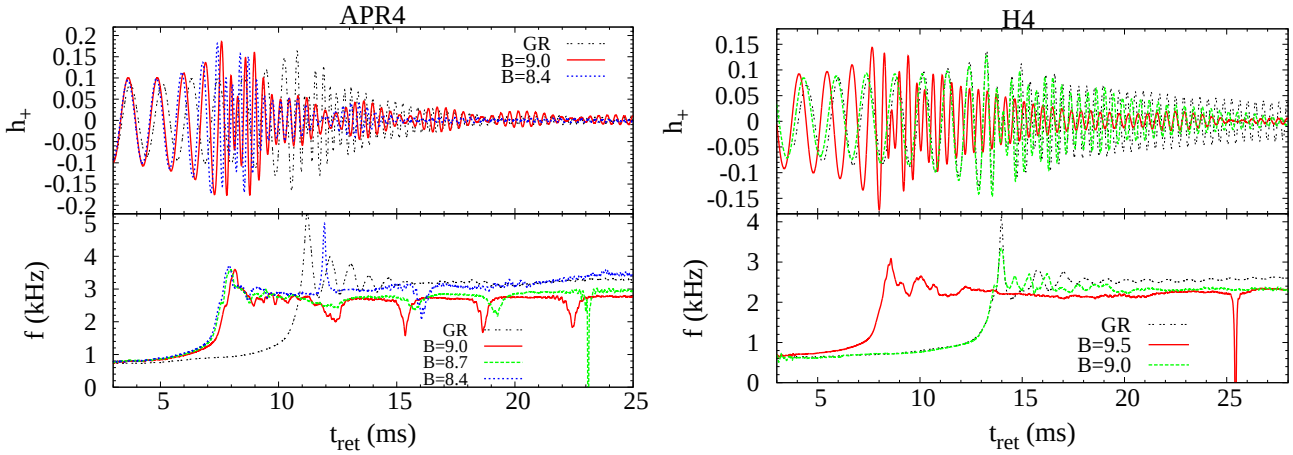

FIG. 4. We show plus-polarization gravitational waves observed along the axis perpendicular to the orbital plane and the frequency of gravitational waves as functions of the retarded time for $m = 2.7M_\odot$ for the APR4 EOS (left panel) and the H4 EOS (right panel). We note that when spikes occur in the frequency plots (at $t_{\rm ret} \approx 23$ ms for $B = 8.7$ in the left panel and at $t_{\rm ret} \approx 26$ ms for $B = 9.5$ in the right panel), the amplitude of the gravitational waves is too low to accurately determine the frequency.

fact that the amount of scalarization is enhanced with the decrease of the orbital separation.

- For $B = 8.0$ with the APR4 EOS and for $B = 8.0-9.0$ with the H4 EOS, the scalarization occurs *after* the onset of the merger. (We note that for $B = 7.5$ with the APR4 EOS, the scalarization does not occur and hence the entire evolution is approximately the same as that in the general-relativistic case.) The maximum density of the scalarized massive neutron star formed after the merger is significantly different from that of nonscalarized or general-relativistic cases. This implies that the structure of the scalarized remnant massive neutron star is also quite different from the nonscalarized neutron star.

- For relatively small values of B, the amplitude of the scalar field of scalarized remnant massive neutron stars decreases with time because their density increases, and eventually, the scalar field approaches zero (see the curves for $B = 8.4$ with the APR4 EOS and $B = 8.0$ with the H4 EOS). This is due to the fact that relativistic effects become so strong during the evolution of the remnant massive neutron star that the scalarization is turned off (see Sec. III A).

The reason of why the scalarization occurs after the onset of the merger, even for relatively small values of B, may be explained using the analysis of Sec. III A. Indeed, we have found there that the scalarization is likely to occur for $(-BT)^{1/2}R \to \pi/2$. Here, R denotes the stellar radius. This implies that even for a small value of BT, the scalarization can occur for a large value of R or a large value of the compactness, $\sqrt{-T}R \sim \sqrt{M/R}$ where M is the mass of the remnant massive neutron star. The compactness of the massive neutron star of mass $\sim 2.6M_\odot$ is larger, by several 10%, than the compactness of a spherical neutron star of mass $1.35M_\odot$. Thus, even for a small value of B for which the scalarization cannot occur for an isolated neutron star, the scalarization may occur when the massive neutron star is formed as a remnant.

In addition, we find that the lifetime of remnant massive neutron stars can be significantly changed by the scalarization. For the H4 EOS with $m = 2.7M_\odot$, the lifetime is several 10 ms and hence relatively short in general relativity [27]. This is also the case when $B = 8.0$ for the H4 EOS. In these cases, the angular momentum of the massive neutron stars is primarily reduced by the angular-momentum transport to the outer material, which is induced by the torque exerted by the massive neutron star of an ellipsoidal figure. After substantial spin-down, the massive neutron star collapses to a black hole. By contrast, in the presence of scalarization (e.g., $B \gtrsim 8.5$), the massive neutron star relaxes to a quasistationary state of a smaller degree of nonaxisymmetry. This seems to indicate that the scalar field contributes to the redistribution of angular momentum. The scalarized massive neutron stars seem to possess high angular momentum but the profile is not significantly nonaxisymmetric. Because these massive neutron stars are hypermassive, they will collapse eventually to a black hole by some dissipation or transport processes of angular momentum. However, the lifetime seems to be much longer than that in general relativity.

Before ending this section, we briefly comment on the mass ejection that could be a source of transient electromagnetic signals (e.g., see Ref. [50]). Since the merger dynamics is modified by the scalar field, we expect that the amount of ejected material is also modified. For the APR4 EOS, the scalarized massive neutron stars formed after the merger is less compact than that in general relativity (see Fig. 3). In addition, the amplitude of the quasiradial oscillations, which enhance angular-momentum transport, are lower. Because of these effects, the total amount of ejected mass is slightly decreased. Indeed, Ref. [36] found that compact massive neutron stars with high oscillation amplitude produce larger mass ejection. In general relativity, an equal-mass binary with $m = 2.7M_\odot$ ejects a mass of $\sim 7 \times 10^{-3}M_\odot$ [36] while we find

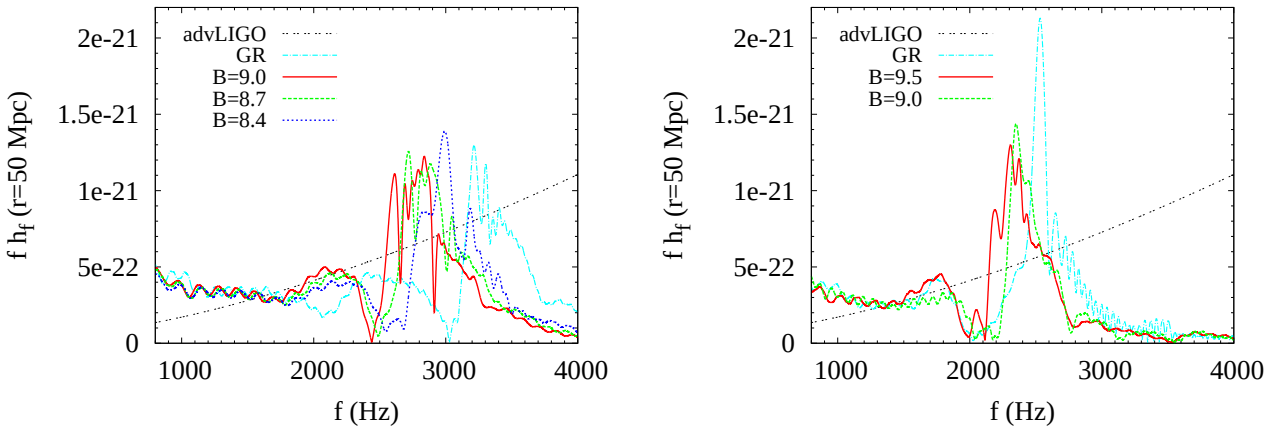

FIG. 5. The Fourier spectrum of gravitational waveforms for the APR4 EOS (left panel) and the H4 EOS (right panel). We assume that gravitational waves are observed along the axis perpendicular to the orbital plane. The black dot-dot curve is the noise spectrum ($\sqrt{fS_n(f)}$ with $S_n(f)$ being the noise power spectrum) of the advanced LIGO with an optimistic configuration for the detection of high-frequency gravitational waves (the so-called zero-detuned high-power case: see https://dcc.ligo.org/cgi-bin/DocDB/ShowDocument?docid=2974).

that for $B = 9.0$, the mass ejected is $\sim 5\times10^{-3}M_\odot$. Thus, the effect is mild. By contrast, the effect is significant for the H4 EOS. In this case, the total amount of ejected mass is quite small in general relativity $\sim 5\times10^{-4}M_\odot$. However in the scalar-tensor theory, it becomes $\sim 5\times10^{-3}M_\odot$ for $B = 9.5$ and $\sim 2\times10^{-3}M_\odot$ for $B = 9.0$. A possible reason of this finding is that due to scalarization, the massive neutron star becomes more compact and hence the effect of shock heating is enhanced and more material is ejected.

B. Gravitational-wave characteristics

As a result of the modification of the dynamical motion induced by the scalarization, gravitational waveforms are also modified. We show in Fig. 4 the gravitational waveforms and the corresponding frequencies for several values of B and for the APR4 EOS (left panel) and the H4 EOS (right panel). We also show the Fourier spectrum of these gravitational waves in Fig. 5 at a distance of 50Mpc. As described above and also found in Ref. [21], the inspiral stage shortens when the neutron stars are scalarized, e.g., typically the number of gravitational-wave cycles in the scalarized case is smaller than in the general-relativistic case by 2–4 cycles. We obtain this reduction simulating a binary evolution that is not very long. The difference in number of cycles between the scalarized and general-relativistic cases would increase for much longer waveforms. Long, accurate evolutions are beyond the scope of this paper. They will be investigated in the future using also comparisons with post-Newtonian models. Thus, in the following we focus on the merger waveforms.

The modification of the waveform emitted by a massive neutron star formed after the merger is quite evident even for relatively small values of $B \gtrsim 8.0$ both for the APR4 and H4 EOSs. However, the way in which the merger waveform is modified depends on the EOS. For the APR4 EOS, we find that a scalarized remnant massive neutron star is less compact than a massive neutron star in general relativity. As a result, the frequency of quasiperiodic gravitational waves is significantly (down to ~ 0.5 kHz) decreased due to the scalarization (see Fig. 5). In general relativity, the peak frequency is 3.2–3.3 kHz while for $B = 9.0$, it is much lower 2.6–2.8 kHz. We also note that the spectrum around the peak is rather wide for the large values of $B \sim 9.0$. This reflects the fact that the frequency of quasiperiodic gravitational waves varies with time.

For the H4 EOS, the scalarized massive neutron star formed after merger is more compact than the one in general relativity. However, the frequency of quasiperiodic gravitational waves does not become higher; rather, it becomes slightly lower due to the scalarization. This indicates that not only the compactness but also the presence of the high-amplitude scalar field plays an important role for determining the oscillation-mode frequency. For the H4 EOS, it is also remarkable that the damping time scale of the wave amplitude for the scalarized case is shorter than in general relativity. The reason for this is that the ellipticity of the massive neutron star decreases in a shorter time scale for the scalarized case.

It is worth to emphasize that these modifications are seen even in the case for which the scalarization does not occur during the inspiral stage. For such cases, the inspiral signal is not modified and cannot be used to constrain the scalar-tensor theory. For such a small value of B, the effects of the scalar field cannot be observed in standard neutron stars, as well, and in the next section we shall discuss some implications of these findings.

In addition to gravitational waves, scalar waves [3] produced by the scalar field φ can carry away nonnegligible energy from the system. However, we find that the energy emitted is a small fraction of the total energy dissipated. For example,

[3] Those scalar waves should not be confused with the scalar mode of gravitational waves in a scalar-tensor theory.

for the APR4 EOS with $B = 9.0$, we find that scalar waves are emitted in both the late inspiral and merger stages. Even for this case, the total energy emitted in scalar waves is only $\sim 3\%$ of that emitted in gravitational waves. For the case of smaller values of B, this fraction is smaller. The primary reason for this small contribution is that for the equal-mass case, the dipole radiation is absent, and the main contribution comes only from the monopole and quadrupole radiation. Therefore, the gravitational-wave emission primarily determines the evolution of the binary system during the inspiral stage, even if the scalarization occurs during the late inspiral stage.

V. SUMMARY AND DISCUSSION

In this paper we used numerical-relativity simulations to investigate the late inspiral and merger dynamics and the gravitational-wave emission of binary neutron stars in a scalar-tensor theory that admits spontaneous scalarization [11–13].

We confirmed, through several numerical-relativity simulations, what was suggested in Ref. [21], notably that if one or both neutron stars are not initially spontaneously scalarized, they can be scalarized dynamically during the late inspiral stage due to nonlinear interactions of the scalar field configuration (see also Ref. [23] for more details). After the scalarization sets in, the inspiral is accelerated and the total number of gravitational-wave cycles is significantly decreased with respect to the general-relativistic case. Given the mass of the neutron star, its EOS and the constraints from binary pulsar observations, we determined for which values of B dynamical scalarization occurs. For example for $M_{\rm NS} = 1.35 M_\odot$, we found for the APR4 EOS, $8 \lesssim B \lesssim 9$, while for the H4 EOS, we found only a very narrow window in the vicinity of $B \sim 9.0$ where the neutron stars in a binary system are dynamically scalarized before coalescing. These results imply that even if the DEF scalar-tensor theory may give deviations to general relativity that are not detected by observations of binary systems at large separations, i.e., in the weak-field regime (pulsar timing observations), nevertheless, the binary system may undergo dynamical scalarization during the last stages of inspiral, i.e., in the strong-field regime, and produce larger deviations to general relativity which could be detected by ground-based gravitational-wave detectors. Further studies, which make use of longer numerical-relativity waveforms, analytical templates to model them, and data-analysis techniques of the kind employed in Ref. [62], will address and assess the interesting possibility of observing such deviations to general relativity with ground-based detectors.

Furthermore, we found that the scalarization can occur even after the onset of the merger. The reason is that the newly formed, massive neutron star can have larger compactness, and hence, the scalarization can occur even for small values of B for which standard-mass neutron stars cannot be scalarized in a binary system (see Sec. III A). We also found that the subsequent evolution of the remnant massive neutron star is quantitatively different from that in general relativity. When the remnant massive neutron star is scalarized, the compactness is different from that in general relativity and the frequency of quasiperiodic gravitational waves is modified. The modification depends on the EOS. For the APR4 EOS, the remnant massive neutron stars are less compact and the frequency of the quasiperiodic oscillations is in general lower. By contrast for the H4 EOS, the remnant is only slightly more compact and the frequency of the quasiperiodic oscillations is not significantly modified. Furthermore, the scalarization seems to enhance the redistribution of angular momentum. In fact, we found that for scalarized massive neutron stars, which are in general nonaxisymmetric, the time scale of the decrease of the ellipticity of the massive neutron star is shorter than in general relativity. As a consequence of this effect, the gravitational-wave amplitude decreases with a shorter time scale, and in addition, the life time of the massive neutron star is increased.

For the case the scalarization occurs only after the merger, the inspiral signal is the same as that in general relativity and cannot be used to constrain the scalar-tensor theory. Nevertheless, we found that quasiperiodic gravitational waveforms from the scalarized, massive neutron stars are different from those in the general-relativistic case. References [26, 27] discussed the possibility that the EOS of neutron stars can be constrained by observing the frequency of those quasiperiodic gravitational waves emitted by remnant massive neutron stars. Assuming that general relativity is correct, this method could be useful. However, our results showed that if general relativity is slightly violated, the method proposed in Refs. [26, 27] alone is not sufficient to extract the EOS because the frequency of quasiperiodic gravitational waves emitted by remnant massive neutron stars depends not only on EOS but also on the degree of scalarization.

Nevertheless, the results found in this paper suggest a new way of testing general relativity. When B is such that spontaneous and dynamical scalarization does not set in before merger or they are very weak, then the inspiral signal is not modified significantly, and the EOS can be determined from the inspiral stage by observing finite-size effects in binary neutron stars [51–59]. If for those values of B, the merger signal is modified because the newly, formed neutron star is sufficiently massive to be scalarized and one finds that the characteristic frequency of quasiperiodic gravitational waves agrees with the prediction of general relativity, then one would conclude that general relativity is correct also in the strong field regime. However, if the characteristic frequency does not agree with the general-relativity prediction, then one would find that general relativity is violated. The success of this test depends crucially on the sensitivity of the gravitational-wave detectors at frequencies between 400 Hz and ~ 4 kHz, on the statistical significance of the quasiperiodic oscillations in the merger waveform and on the possibility of producing numerical-relativity waveforms in scalar-tensor theory with systematic errors smaller than statistical ones.

ACKNOWLEDGMENTS

We thank Enrico Barausse and Gilles Esposito-Farése for useful discussions. This work was supported by Grant-

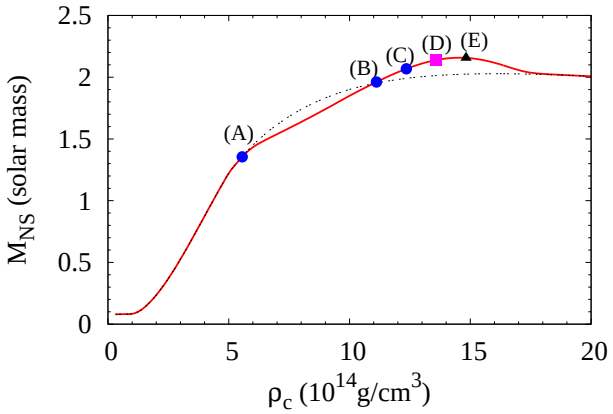

FIG. 6. The neutron-star mass as a function of the central density ρ_c for spherical neutron stars with the H4 EOS with $B = 10$ and $\varphi_0 = 3 \times 10^{-3}$. The solid and dashed curves show the relation in a scalar-tensor theory and in general relativity, respectively.

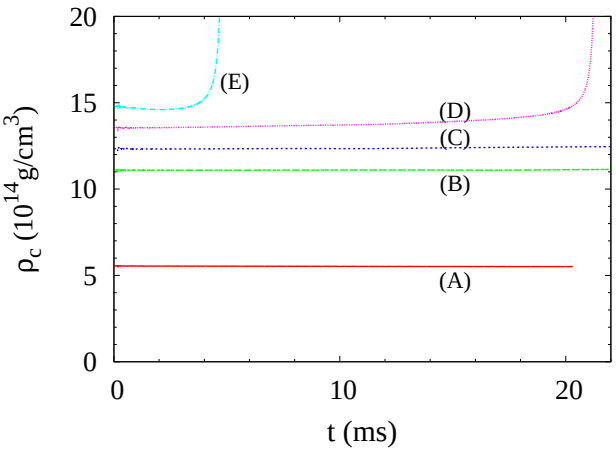

FIG. 7. Evolution of the central density ρ_c for five spherical neutron stars. Curves from bottom to top show the results for (A) to (E), respectively.

in-Aid for Scientific Research (24244028), by Grant-in-Aid for Scientific Research on Innovative Area (20105004), and HPCI Strategic Program of Japanese MEXT. H.O. acknowledges financial support provided under the European Unions FP7 ERC Starting Grant "The dynamics of black holes: testing the limits of Einstein's theory" grant agreement no. DyBHo256667. A.B. acknowledges partial support from NSF Grant No. PHY-1208881 and NASA Grant NNX09AI81G. A.B. also thanks for hospitality in the longterm workshop on *Gravitational Waves and Numerical Relativity* held at the Yukawa Institute for Theoretical Physics, Kyoto University in May and June 2013.

Appendix A: Numerical simulations of isolated, spherical neutron stars

To check the validity of our newly developed numerical-relativity code for binary neutron stars in scalar-tensor theories, we perform simulations of isolated, spherical neutron stars in scalar-tensor theories. We prepare spherical neutron stars using a piecewise polytropic EOS (see, e.g., Ref. [36] for details). We perform many simulations varying the EOS and find that our conclusions are essentially the same irrespective of the chosen EOS. For this reason, here we focus on the results with the H4 EOS, which is a rather stiff EOS, with the maximum mass of a spherical neutron star in general relativity being $\approx 2.03 M_\odot$ (see Fig. 6).

To show that our code works properly also in the case the coupling between the scalar and tensor fields is strong, we choose $B = 10$ and $\varphi_0 = 3 \times 10^{-3}$, even if those values are not realistic because they were already excluded by the observation of neutron star-white dwarf binaries (see Sec. III). For this choice of the parameters, we plot in Fig. 6 the neutron-star (tensor) mass as a function of the central density in general relativity and in the scalar-tensor theory under investigation. As we see from Fig. 6, the mass in scalar-tensor theory starts differing from the one in the general-relativistic case for $\rho_c \gtrsim 5 \times 10^{14}\,\mathrm{g/cm^3}$ (or for $M \gtrsim 1.35 M_\odot$). We find that this difference is a consequence of the fact the scalar field is significantly excited, resulting in the modification of the density profile of the neutron star. When the central density is extremely high, $\rho_c \gtrsim 1.8 \times 10^{15}\,\mathrm{g/cm^3}$, the neutron star in general relativity and the scalar-tensor theory agrees with each other approximately. The reason is that $T(= T_a{}^a)$ becomes positive in this density range, and thus the scalar mass becomes much smaller than the neutron-star mass (see Sec. III A). We also find that in the scalar-tensor theory, the maximum mass is $\approx 2.2 M_\odot$, that is larger than in the general-relativistic case. The fraction of increase depends strongly on the value of B as well as φ_0. All those properties are universal and qualitatively independent on the EOS.

We perform numerical simulations using five neutron stars, for which the central density and neutron-star mass are plotted in Fig. 6 (with labels (A) – (E)). The neutron stars (A) – (C) are expected to be stable, while (D) and (E) could be unstable; in particular for (E), it is reasonable to expect that it is unstable because the central density is larger than that of the neutron star with the maximum mass.

We plot in Fig. 7 the evolution of the central density for the five neutron stars. Note that the dynamical time scale of these neutron stars defined by $\rho_c^{-1/2}$ is shorter than 0.2 ms, and hence, the simulations run for a time much longer than the dynamical time scale. As expected, the neutron stars (A) – (C) (having lower central density) are stable; the central density (as well as the stellar structure) is unchanged in the simulation time. By contrast, for (E), the star collapses to a black hole in a short time scale. Therefore, we conclude that it is unstable against the radial oscillation.

The stability of (D) is not very clear. In our simulation, this star always collapses to a black hole in the time scale of 10 milliseconds. However, the lifetime depends strongly on the

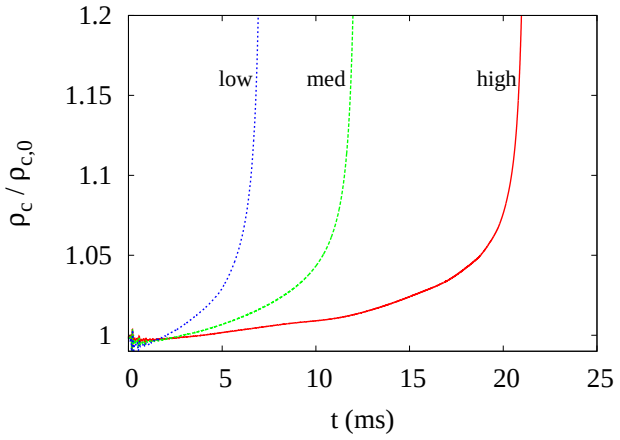

FIG. 8. Evolution of the central density for neutron star (D) (see Fig. 6) with three different grid resolutions. The dotted, dashed, and solid curves show the results for low, medium, high resolutions, respectively, with the grid spacing, 0.369, 0.295, and 0.236 km.

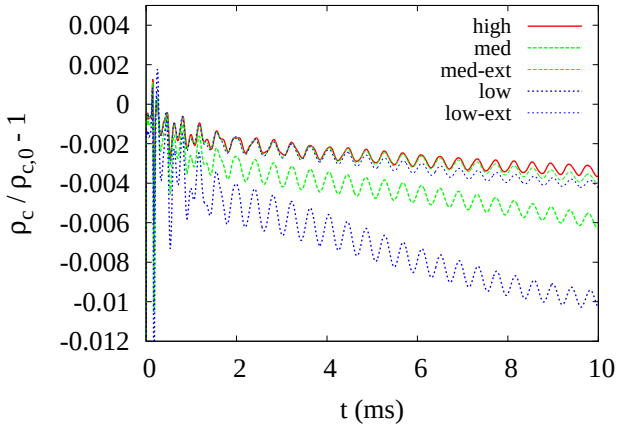

FIG. 9. Evolution of the central density for neutron star (A) (see Fig. 6) with three different grid resolutions. Here, $\rho_c/\rho_{c,0}-1$ is plotted with $\rho_{c,0}$ being the central density at $t=0$. The dotted, dashed, and solid curves show the results for low, medium, and high resolutions, respectively, with the grid spacing, 0.461, 0.369, and 0.295 km. The thin curves are plotted extrapolating the results of the low and medium resolution runs under the assumption of second-order convergence.

grid resolution. In Fig. 8 we plot the evolution of the central density for (D) with three different grid resolutions. We find that the lifetime significantly increases as we improve the grid resolution. Thus, we cannot draw a strong conclusion for the stability to this neutron star. This finding is not surprising because the star (D) is located in the vicinity of the maximum mass along the equilibrium sequence and thus it is likely that this star is approximately equal to a marginally stable star.

By contrast, the convergence of the numerical results is achieved in a much better manner for the evolution of stable neutron stars. In Fig. 9 we plot the evolution of the central density for (A) with three different grid resolutions. Note that for this star, the mass is approximately $1.35M_\odot$, i.e., approximately equal to the neutron-star mass considered in this paper. We find that due to the numerical error, the central density gradually decreases with time, but with improving grid resolution, such numerical effects become smaller. To find the order of convergence, we also plot $(\rho_c/\rho_{c,0}-1)(\Delta x_{\rm high}/\Delta x)^2$ where Δx is the grid spacing and $\Delta x_{\rm high}$ is Δx for the high resolution run. We show in Fig. 9 that this quantity agrees approximately with $\rho_c/\rho_{c,0}-1$ for the high-resolution run. This implies that the error convergences approximately at second order.

Finally, we show that we can accurately follow in our code the black hole formation and evolution. In Fig. 10 we plot the evolution of the irreducible mass defined by $\sqrt{A_{\rm AH}/16\pi}$ where $A_{\rm AH}$ is the area of the apparent horizon for neutron star (E) in units of the initial ADM mass. Note that the ADM mass is not equal to the tensor mass (neutron-star mass) and for this neutron star, the initial Komar and tensor masses are 0.6% and 0.3% larger than the initial ADM mass. After the formation of the black hole, the scalar mass is lost, and hence, the mass of the black hole approaches the initial ADM mass. We show in Fig. 10 that the final black hole mass agrees with the initial ADM mass within 0.1% for the high-resolution run. Thus, the final mass does not agree with the initial Komar mass nor the initial tensor mass. This indicates that our code can follow the black hole accurately.

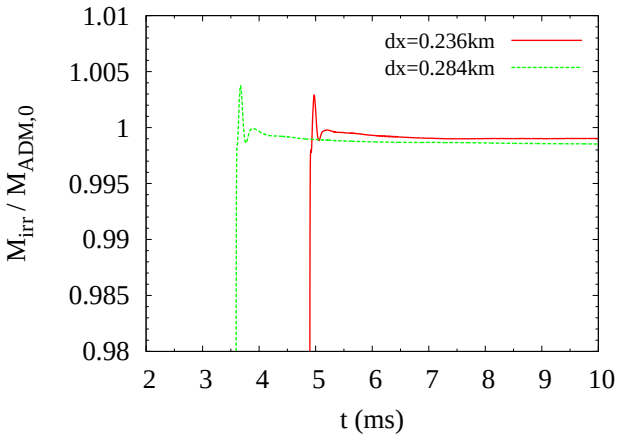

FIG. 10. Evolution of the irreducible mass defined by $\sqrt{A_{\rm AH}/16\pi}$ where $A_{\rm AH}$ is the area of the apparent horizon for star (E) (see Fig. 6) in units of the initial ADM mass.

It is also worth to note that the irreducible mass *decreases* with time in the early stage of the black hole evolution. In general relativity, this is not allowed. However, this is reasonable in the present case because in the Jordan frame, the null energy condition can be violated due to the presence of the scalar field, as pointed out in Ref. [60].

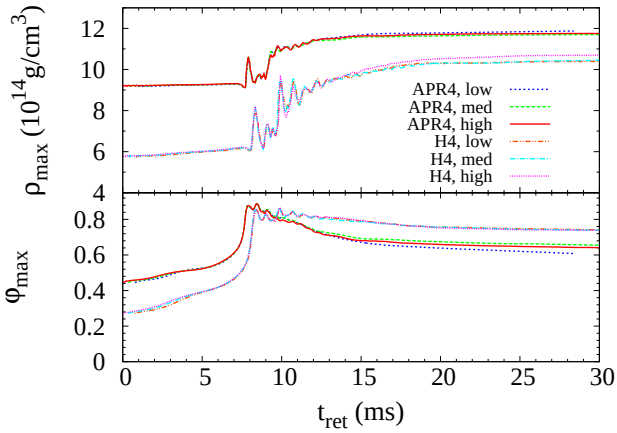

FIG. 11. The same as Fig. 3 for the APR4 EOS with $B = 9.0$ and $\varphi_0 = 10^{-5}$ and for the H4 EOS with $B = 9.5$ and $\varphi_0 = 5 \times 10^{-5}$ but for three different grid resolutions. We align the waveforms at the merger time by shifting the curves at low and medium resolutions by approximately $+0.7$ and $+0.3$ ms, respectively.

Appendix B: Convergence of numerical results

Here we want to discuss the convergence of the numerical-relativity simulations.

To check the convergence, we consider simulations for the APR4 EOS with $B = 9.0$ and $\varphi_0 = 10^{-5}$ and for the H4 EOS with $B = 9.5$ and $\varphi_0 = 5 \times 10^{-5}$. We perform runs using three grid resolutions. For low, medium, and high resolutions, the stellar diameter at the initial stage is covered approximately by 67, 80, and 100 grid points, respectively.

In Fig. 11 we plot the evolution of the maximum density and the maximum value of φ for three grid resolutions. As often found in the simulations of inspiraling neutron stars, a lower grid resolution always results in shorter merger time because of the larger numerical dissipation. To align the merger time, we shift the curves of low and medium resolutions approximately by $+0.7$ and $+0.3$ ms, respectively. Although the inspiral duration is modified by the numerical effect, Fig. 11 shows that the merger dynamics depends only weakly on the grid resolution. Thus, for drawing the conclusions in our paper, we can assume that we achieved convergence.

We plot in Fig. 12 the gravitational waveform and the corresponding frequency for the APR4 EOS with $B = 9.0$ and for the H4 EOS with $B = 9.5$. Again, the time is shifted to align the waveforms at merger. The waveforms computed with the three grid resolutions agree qualitatively well, with the agreement being the best with the H4 EOS. For the early merger stage (i.e., in the first ~ 5 ms after the onset of the merger), the agreement is quantitatively better independently on the EOSs. For the later merger stage, the agreement becomes poorer, because the dynamics in the merger stage depends strongly on the efficiency of shock heating for which the convergence is achieved only at first order. Nevertheless, the characteristic frequency of gravitational waves depends only weakly on the grid resolution. We find that the disagreement is within ~ 0.1 kHz for the APR4 EOS and within ~ 0.05 kHz or less for the H4 EOS. Those differences are much smaller than the differences from the general-relativity results. We find that the convergence for the H4 EOS is much better than that for the APR4 EOS. The possible reason for this is that neutron stars with the H4 EOS are less compact and shock heating effects are weaker with this EOS.

Finally, we extracted these gravitational waves at the finite radii $\approx 200-400$ km and we did not extrapolate the waveforms at infinity because we expect that the numerical error due to the extraction at finite radius is smaller than the one due to resolution (see Refs. [61]).

[1] J. Abadie, et al., Nucl. Instrum. Meth. **A624**, 223 (2010); T. Accadia, et al., Class. Quantum Grav. **28**, 025005 (2011); K. Kuroda, et al., Class. Quantum Grav. **27**, 084004 (2010).
[2] V. Kalogera et al., Phys. Rep. **442**, 75 (2007).
[3] J. Abadie et al. (The LIGO Scientific Collaboration and Virgo Collaboration), Class. Quantum Grav. **27**, 173001 (2010).
[4] J. Aasi et al. (The LIGO Scientific Collaboration and Virgo Collaboration), arXiv:1304.0670 [gr-qc] (submitted to Living Review in Relativity).
[5] P. Jordan, Nature **164**, 637 (1949); Z. Phys. **157**, 112 (1959).
[6] M. Fierz, Helv. Phys. Acta **29**, 128 (1956).
[7] C. Brans and R. H. Dicke, Phys. Rev. **124**, 925 (1961).
[8] C. M. Will, *Theory and experiment in gravitational physics* (Cambridge University Press, 1992).
[9] C. M. Will, Living Review in Relativity, **9**, 3 (2006).
[10] B. Bertotti, L. Iess, and P. Tortora, Nature **425**, 374 (2003).
[11] T. Damour and G. Esposito-Farése, Phys. Rev. Lett. **70**, 2220 (1993)
[12] T. Damour and G. Esposito-Farése, Class. Quantum Grav. **9**, 2093 (1992).
[13] T. Damour and G. Esposito-Farése, Phys. Rev. D **53**, 5541 (1996); Phys. Rev. D **54**, 1474 (1996); Phys. Rev. D **58**, 042001 (1998).
[14] T. Sotiriou and V. Faraoni, Rev. Mod. Phys. **82**, 451 (2010).
[15] T. Jacobson and D. Mattingly, Annals Phys. **321**, 150 (2006).
[16] T. Jacobson, arXiv:0801.1547 [gr-qc]; K. Yagi *et al.* arXiv:1307.6219 [gr-qc].
[17] D.M. Eardley, Astrophys. J. **196**, L59 (1975).
[18] C.M. Will and H.W. Zaglauer, Astrophys. J. **346**, 366 (1989).
[19] S. Mirshekari and C. Will, Phys. Rev. D **87**, 084070 (2013).
[20] J. Healy *et al.*, arXiv:1112.3928 [gr-qc].
[21] E. Barausse, C. Palenzuela, M. Ponce, and L. Lehner, Phys. Rev. D **87**, 081506 (R) (2013).
[22] E. Berti *et al.* Phys.Rev. D **87**, 124020 (2013).
[23] K. Taniguchi, M. Shibata, and A. Buonanno (inpreparation).
[24] P. C. C. Freire, N. Wex, G. Esposito-Farése, J. P. W. Verbiest, M. Bailes, B. A. Jacoby, M. Kramer, I. H. Stairs, J. Antoniadis, and G. H. Janssen, Mon. Not. R. Soc. Astron. **423**, 3328 (2012).
[25] J. Antoniadis et al., Science **340**, 448 (2013).
[26] A. Bauswein and H.-Th. Janka, Phys. Rev. Lett. **108**, 011101

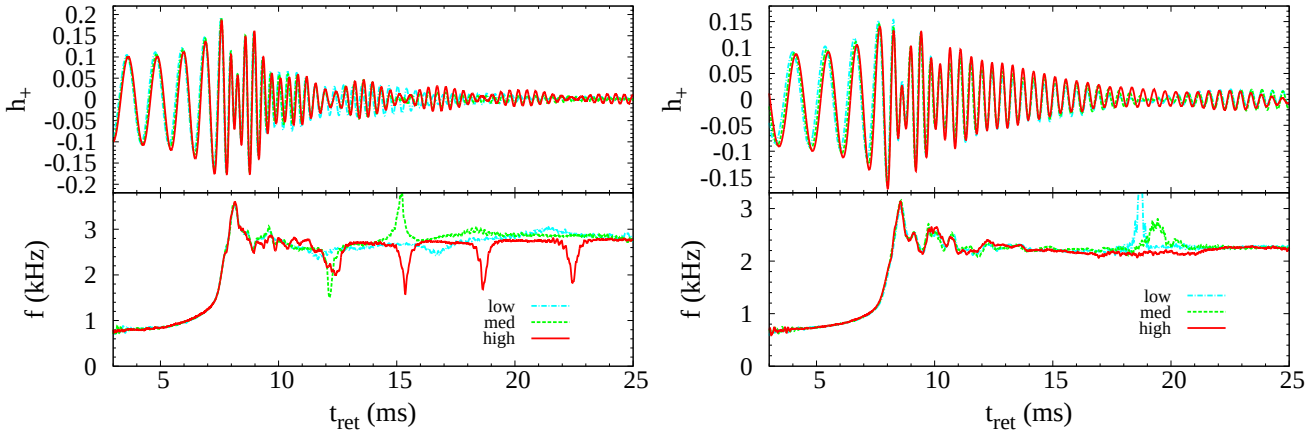

FIG. 12. The same as Fig. 4 for the APR4 EOS with $B = 9.0$ and $\varphi_0 = 10^{-5}$ and for the H4 EOS with $B = 9.5$ and $\varphi_0 = 5 \times 10^{-5}$ but for three different grid resolutions. We align the merger time by shifting the curves of low and medium resolution by approximately $+0.7$ and $+0.3$ ms, respectively.

(2012); A. Bauswein, H.-Th. Janka, K. Hebeler, and A Schwenk, Phys. Rev. D **86**, 063001 (2012).
[27] K. Hotokezaka, K. Kiuchi, K. Kyutoku, T. Muranushi, Y. Sekiguchi, M. Shibata, and K. Taniguchi, Phys. Rev. D **88**, 044026 (2013).
[28] M. Shibata and T. Nakamura, Phys. Rev. D **52**, 5428 (1995).
[29] T.W. Baumgarte and S. L. Shapiro, Phys. Rev. D **59**, 024007 (1998).
[30] S. Brandt and B. Brügmann, Phys. Rev. Lett. **78**, 3606 (1997).
[31] M. Campanelli, C. O. Lousto, and P. Marronetti, and Y. Zlochower, Phys. Rev. Lett., **96**, 111101 (2006).
[32] J. G. Baker, J. Centrella, D.-I. Choi, M. Koppitz, and J. van Meter, Phys. Rev. Lett. **96**, 111102 (2006).
[33] T. Yamamoto, M. Shibata, and K. Taniguchi, Phys. Rev. D **78**, 064054 (2008).
[34] B. Brügmann, J. A. González, M. Hannam, S. Husa, U. Sperhake, and W. Tichy, Phys. Rev. D **77**, 024027 (2008).
[35] A. Kurganov and E. Tadmor, J. Comput. Phys. **160**, 241 (2000).
[36] K. Hotokezaka, K. Kiuchi, K. Kyutoku, H. Okawa, Y. Sekiguchi, M. Shibata, and K. Taniguchi, Phys. Rev. D **87**, 024001 (2013).
[37] A. Bauswein, H.-Th. Janka, and R. Oechslin, Phys. Rev. D **82**, 084043 (2010).
[38] A. Akmal, V. R. Pandharipande, and D. G. Ravenhall, Phys. Rev. D **58**, 1804 (1998).
[39] N. K. Glendenning and S. A. Moszkowski, Phys. Rev. Lett. **67**, 2414 (1991); B. D. Lackey, M. Nayyar, B. J. Owen, Phys. Rev. D **73**, 024021 (2006).
[40] P. Demorest, T. Pennucci, S. Ransom, M. Roberts, and J. Hessels, Nature **467**, 1081 (2010).
[41] J. A. Isenberg, Int. J. Mod. Phys. D **17**, 265 (2008); J. R. Wilson and G. J. Mathews, Phys. Rev. Lett. **75**, 4161 (1995).
[42] S. A. Teukolsky, Astrophys. J. **504**, 442 (1998); M. Shibata, Phys. Rev. D **58**, 024012 (1998).
[43] http://www.lorene.obspm.fr/.
[44] G. Esposito-Farése, arXiv:gr-qc/0402007.
[45] D. L. Lee, Phys. Rev. D **10**, 2374 (1974).
[46] A. Komar, Phys. Rev. **113**, 934 (1959).
[47] M. Shibata and K. Kawaguchi, Phys. Rev. D **87**, 104031 (2013).
[48] C. M. Will and H. W. Zaglauer, Astrophys. J. **346**, 366 (1989).
[49] H. Müller and B. D. Serot, Nucl. Phys. A **606**, 508 (1996).
[50] L. Li and B. Paczyński, Astrophys. J. **507**, L59 (1998); S. R. Kulkarni, astro-ph:0510256; B. D. Metzger, G. Martinez-Pinedo, S. Darbha, E. Quataert, A. Arcones, D. Kasen, T. Thomas, P. Nugent, I. V. Panov, and N. T. Zinner, Mon. Not. Roy. Soc. **406**, 2650 (2010); B. D. Metzger and E. Berger, Astrophys. J. **746**, 48 (2012); T. Piran, E. Nakar, and S. Rosswog, Mon. Not. R. Soc. Astro. **430**, 2121 (2013); J. Barnes and D. Kasen, Astrophys. J. **775**, 18 (2013); M. Tanaka and K. Hotokezaka, Astrophys. J. **775**, 113 (2013).
[51] D. Lai, F. A. Rasio, and S. L. Shapiro, Astrophys. J. **420**, 811 (1994).
[52] E. E. Flanagan, and T. Hinderer, Phys. Rev. D **77**, 021502(R) (2008).
[53] J. S. Read, C. Markakis, M. Shibata, K. Uryu, J. D. E. Creighton, and J. L. Friedman, Phys. Rev. D **79**, 124033 (2009).
[54] T. Hinderer, B. D. Lackey, R. N. Lang, and J. S. Read, Phys. Rev. D **81**, 123016 (2010).
[55] T. Damour, A. Nagar, and L. Villain, Phys. Rev. D **85**, 123007 (2012); D. Bini, T. Damour, and G. Faye, Phys. Rev. D **85**, 124034 (2012).
[56] L. Baiotti, T. Damour, B. Giacomazzo, A. Nagar, and L. Rezzolla, Phys. Lett. **105**, 0261101 (2010); L. Baiotti, T. Damour, B. Giacomazzo, A. Nagar, and L. Rezzolla, Phys. Rev. D **84**, 024017 (2011).
[57] S. Bernuzzi, M. Thierfelder, and B. Brügmann, Phys. Rev. D **85**, 104030 (2012); S. Bernuzzi, A. Nagar, M. Thierfelder, and B. Brügmann, Phys. Rev. D **86**, 044030 (2012).
[58] K. Hotokezaka, K. Kyutoku, and M. Shibata, Phys. Rev. D **87**, 044001 (2013).
[59] J. S. Read, L. Baiotti, J. D. E. Creighton, J. L. Friedman, B. Giacomazzo, K. Kyutoku, C. Markakis, L. Rezzolla, M. Shibata, and K. Taniguchi, Phys. Rev. D (2013).
[60] M. A. Scheel, S. L. Shapiro, and S. A. Teukolsky, Phys. Rev. D **51**, 4236 (1995).
[61] K. Hotokezaka, K. Kyutoku, and M. Shibata, Phys. Rev. D **87**, 044001 (2013).
[62] W. Del Pozzo, T.G.F. Li, M. Agathos, C. Van Den Broeck, and S. Vitale, arXiv:1307.8338 [gr-qc].